

THE FLORIDA STATE UNIVERSITY  
COLLEGE OF ARTS AND SCIENCES

COMPARISON OF MODELLED AND REMOTELY SENSED (NSCAT)  
BOUNDARY LAYER FLOW AND VORTICITY AROUND ISLANDS

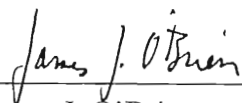
By  
RYAN JAMES SHARP

A Thesis submitted to the  
Department of METEOROLOGY  
in partial fulfillment of the  
requirements for the degree of  
Master of Science

Degree Awarded:

Degree Awarded:  
Fall Semester, 1999

The members of the Committee approve the thesis of Ryan James Sharp defended on September 30, 1999.



---

James J. O'Brien  
Professor Directing Thesis



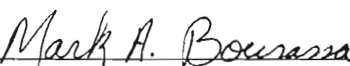
---

Paul H. Ruscher  
Committee Member



---

Tiruvalum N. Krishnamurti  
Committee Member



---

Mark A. Bourassa  
Committee Member

This thesis is dedicated to my wife, Jennifer Sharp, my mother, Kay Sharp, and most importantly, my Lord and Savior, Jesus Christ...

## **ACKNOWLEDGMENTS**

I would like to thank Dr. James O'Brien for his mentorship over the years and also for his guidance in understanding the development of this thesis. I would also like to thank Dr. Mark Bourassa for both his editing skills and his help in understanding NSCAT. Our many discussions were insightful and they helped me to complete this project. I thank my other committee members, Dr's. Paul Ruscher and Tiruvalum Krishnamurti for helping me to add the finishing touches to this thesis. Jason Davey at the Australian Antarctic Division was very generous in support of my research. The majority of the financial support for this research was provided by the National Science Foundation under NSF Grant DGE 9616271. A University Fellowship from Florida State University has helped me to complete this research. Finally, I want to thank my wife, Jennifer Sharp, for her support during this research.

## TABLE OF CONTENTS

List of Figures . . . . .	vii
Abstract . . . . .	ix
1. INTRODUCTION. . . . .	1
a. Heard Island . . . . .	5
b. Previous Findings . . . . .	7
2. MODEL . . . . .	12
a. Stretched Coordinates . . . . .	15
b. Temporal and Spatial Differencing . . . . .	18
c. Boundary Conditions . . . . .	18
d. Model Spinup . . . . .	20
3. CASE STUDIES . . . . .	23
a. Cylindrical Obstacle . . . . .	23
b. Combined Cone and Cylinder Obstacle . . . . .	31
4. DISCUSSION. . . . .	38
5. CONCLUSIONS . . . . .	43
APPENDICES . . . . .	45
A. Coordinate Transformation . . . . .	45
B. Various Necessary Calculations. . . . .	47
1. Calculation of the Layer Wind. . . . .	47
B. Various Necessary Calculations. . . . .	47
1. Calculation of the Layer Wind. . . . .	47
2. Check of the CFL Condition. . . . .	48

C. Scatterometry . . . . .	50
REFERENCES. . . . .	54
BIOGRAPHICAL SKETCH. . . . .	57

## LIST OF FIGURES

<u>Figure</u>	<u>Page</u>
1. Still image taken from the NSCAT gridded wind animations (larger domain animations are publicly available at URL: <a href="http://www.coaps.fsu.edu/scatterometry/">http://www.coaps.fsu.edu/scatterometry/</a> ) for March 15, 1997 at 12:00 UTC. Heard Island is located near latitude 53°S and longitude 73°30'E. Vorticity is contoured and wind speeds are proportional to arrow length. Red (blue) arrows indicate convergence (divergence). . . . .	3
2. Divergence field calculated from the NSCAT gridded winds for March 15, 1997 at 12:00 UTC. Divergence is contoured and the wind speeds are proportional to arrow length. The bins used in gridding the NSCAT wind data are outlined by the dashed lines. . . . .	4
3. Heard Island on a rare clear cloudless day taken by Captain P. Schlossberger of Qantas Airways (photograph courtesy of Australian Antarctic Division). . . . .	6
4. Circular cylinder at R=9.6 (from Van Dyke 1982). It was developed by moving a cylinder through a tank of water containing aluminum powder and illuminated from underneath. <i>Photograph taken by Sadatoshi Taneda.</i> . . . . .	9
5. Model potential-temperature profile (from Lavoie 1974). . . . .	13
6. Flow field around cylindrical obstacle after a spinup of 9 model days. The wind speed is depicted by the background color. The length of the wind arrows is directly proportional to the wind speed. The direction referred to as north in the paper is given in the upper right hand corner. . . . .	24
7. Vorticity field around cylindrical obstacle after a spinup of 9 model days. Note the size of the maxima on each side of the obstacle when compared to the size of the maxima in Fig. 1. Note also the magnitude of the maxima (around $61 \times 10^{-4} \text{ s}^{-1}$ ). . . . .	26
compared to the size of the maxima in Fig. 1. Note also the magnitude of the maxima (around $61 \times 10^{-4} \text{ s}^{-1}$ ). . . . .	26

8.	Divergence field around cylindrical obstacle after a spinup of 9 model days. Note that the maximum divergence in the field is $67 \times 10^{-6} \text{s}^{-1}$ whereas the maximum convergence is $36 \times 10^{-6} \text{s}^{-1}$ . . . . .	28
9.	Boundary layer depth anomaly from the initial state after a spinup of 9 model days. . . . .	29
10.	Flow field around cone/cylinder obstacle after a spinup of 9 model days. The wind speed is depicted by the background color. The length of the wind arrows is directly proportional to the wind speed. The direction referred to as north in the paper is given in the upper right hand corner. . . . .	32
11.	Velocity field difference for the cylinder wind field minus the cone/cylinder wind field. Note the change in magnitude of the color scale. The largest difference is in the area of the maximum winds on the northwest and southwest sides of the obstacle (around $1.2 \text{ms}^{-1}$ faster in the cone/cylinder case than the cylinder case). . . . .	33
12.	Vorticity field difference for the cylinder vorticity minus the cone/cylinder vorticity. Note the change in the magnitude of the color table. Also note that the negative colors on the south side of the domain indicate that the vorticity in the cone/cylinder case are more positive on the south side (and vice versa on the north side). . . . .	36
13.	Divergence field difference for the cylinder divergence minus the cone/cylinder divergence. Notice that the color bar represents values that are an order of magnitude larger than those in the cylinder divergence (Fig. 8). . . . .	37



## ABSTRACT

Examination of NSCAT gridded wind and derivative fields revealed an interesting feature around all small islands in sustained winds. A positive/negative vorticity couplet forms to the right/left of the island with respect to the flow field. Also a convergent/divergent pattern is observed on the windward/leeward side of the island. This is the first time that this type of feature has been observed with a space-borne scatterometer.

The cause of these patterns is investigated with a simple 1.5-layer reduced gravity atmospheric model with parameters similar to the area around Heard Island (a small, isolated island in the Southern Indian Ocean). The model is integrated on a stretched cylindrical coordinate system to highlight features near the island. The eddy diffusivity term ( $K$ ) is a function of the square of the radial distance from the center of the island to account for larger grid spacing at larger radii.

Two case studies are examined utilizing the model. One has a flat bottom topography throughout the domain, with the island represented by a cylindrical wall of infinite height. The second case has an axisymmetric sloping bottom that leads up to a the cylindrical obstacle similar in scale to Heard Island. Results indicate a strong vorticity couplet about three orders of magnitude stronger than that seen by NSCAT, but much closer to the island. The divergence fields in the model and NSCAT gridded vorticity couplet about three orders of magnitude stronger than that seen by NSCAT, but much closer to the island. The divergence fields in the model and NSCAT gridded

products are similar on the windward half of the domain near the island; however, the maximum divergence is located to the right and left of the flow, and it is much weaker behind the island. Possible explanations for these differences are given.

The addition of sloped Heard Island-like topography modified both the vorticity and divergence fields near the island. The vorticity maxima is weakened, but the overall pattern extends further west (on the windward side of the island) thus improving our modelled pattern when compared with observations. The changes in the divergence pattern are focused over the topography with little difference elsewhere.

## 1. INTRODUCTION

In mid-September 1996, the NASA scatterometer (NSCAT) began observing winds over the global oceans. The high temporal and spatial resolution provided by NSCAT (it had the ability to observe about 90% of the ice-free oceans in two days with an in-swath resolution of 25 km) allows for important new meteorological and oceanographical insights. This is particularly true in areas of the globe that previously only had vector wind observations from ERS-1/2 as well as sparse (and less accurate) observations by ships of opportunity. Wind speeds, but not directions, can also be obtained from a host of satellite based remote sensing systems (e.g. the Special Sensor Microwave Imager (SSM/I) and altimetry). However, vector winds allow far more insight into key features of the wind field such as vorticity and divergence.

NSCAT has proven highly accurate in obtaining surface wind speed and direction. NSCAT rms differences are  $1.6 \text{ ms}^{-1}$  and  $13^\circ$  (for correctly selected ambiguities, which occurred for approximately 90% of the vectors) when compared to co-located winds from research vessel observations (Bourassa et al. 1997), and  $1.3 \text{ ms}^{-1}$  and  $18^\circ$  compared to quality-controlled buoy observations (Freilich and Dunbar 1999). This precision at high resolution was an incredible leap forward in our ability to observe the atmosphere. There are many applications in both meteorology and oceanography which will benefit from this technology. Monthly mean surface wind

fields derived from NSCAT observations in coastal and equatorial regions were resolved better than those found by the European Center for Medium-Range Weather Forecasts (ECMWF) operational numerical weather prediction models (Liu et al. 1998). Global daily vector wind products have also been developed (Bourassa et al. 1999; Pegion et al. 1999). Synoptic scale applications, such as quasi-stationary waves in the Southern Hemisphere (Milliff et al. 1999) have also been investigated. NSCAT winds have been used to derive pressure fields and to locate frontal zones (Zierden et al. 1999). NSCAT also gives new insight on meso-scale problems such as the influence of hurricane Marco on the gap flow out of the Chivela Pass (Bourassa et al. 1999). NSCAT winds are valuable for studying wind patterns at a wide range of temporal and spatial scales.

A meso-scale meteorological application is examined herein. Examination of animated NSCAT winds and vorticity (Bourassa et al. 1998, 1999; publicly available at <http://www.coaps.fsu.edu/scatterometry/>) revealed an interesting feature around all small islands (e.g. Taiwan, the islands of the Lesser Antilles, etc.) in sustained winds. This study focuses on a small island in the southern Indian Ocean, Heard Island. When the winds approaching a small island are approximately constant in direction, a positive/negative vorticity couplet forms to the right/left of the island with respect to the flow field (Fig. 1). Also, a divergent (convergent) pattern is detected on the leeward (windward) sides of the island (Figs. 1, 2). This is the first time that there has been sufficient resolution to observe such features without having to set up a small scale observational network. The animations employ a highly weighted temporal averaging observational network. The animations employ a highly weighted temporal averaging

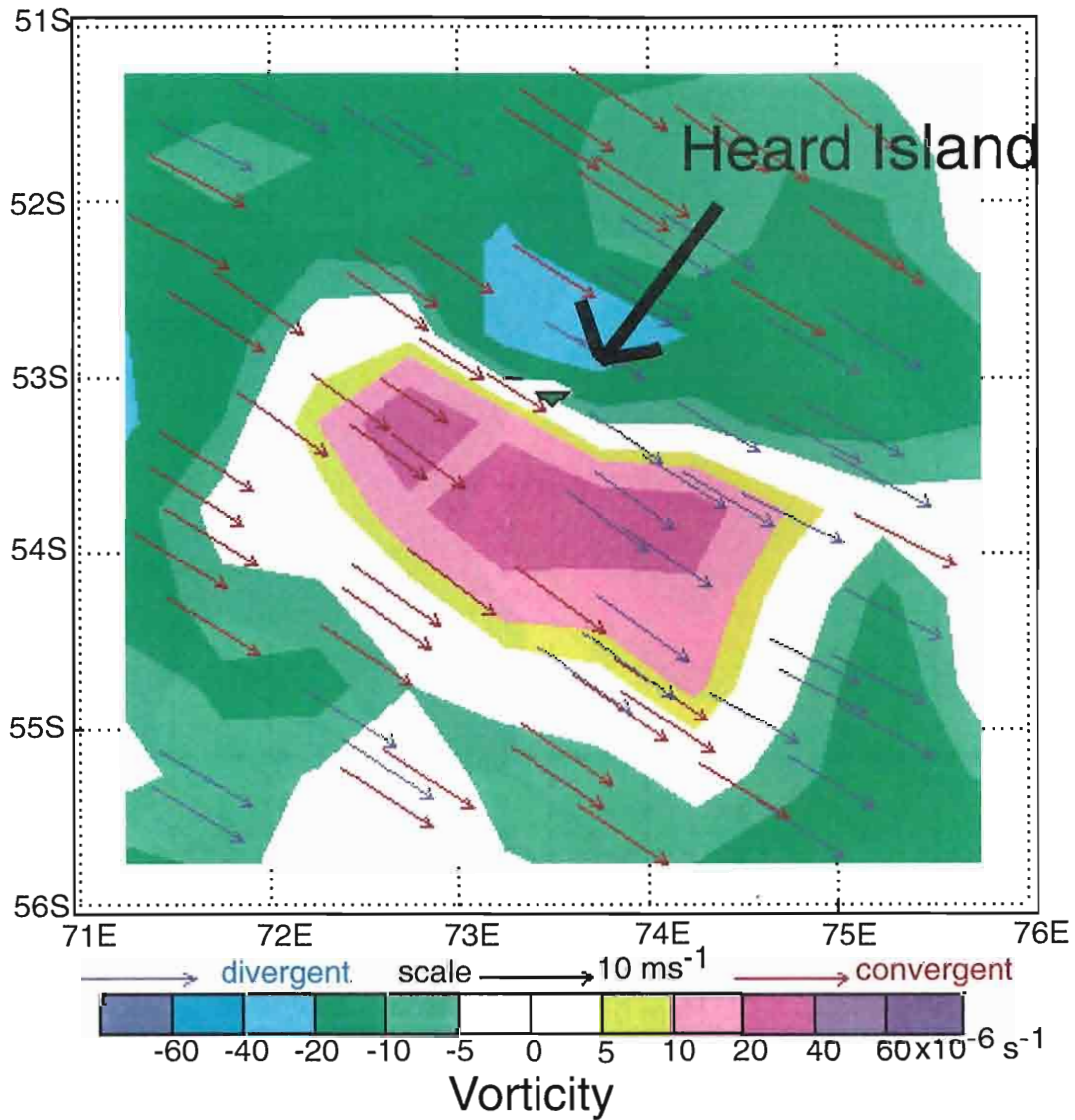


Fig. 1: Still image taken from the NSCAT gridded wind animations (larger domain animations are publicly available at URL: <http://www.coaps.fsu.edu/scatterometry/>) for March 15, 1997 at 12:00 UTC. Heard Island is located near latitude  $53^{\circ}\text{S}$  and longitude  $73^{\circ}30'\text{E}$ . (larger domain animations are publicly available at URL: <http://www.coaps.fsu.edu/scatterometry/>) for March 15, 1997 at 12:00 UTC. Heard Island is located near latitude  $53^{\circ}\text{S}$  and longitude  $73^{\circ}30'\text{E}$ . Vorticity is contoured and wind speeds are proportional to arrow length. Red (blue) arrows indicate convergence (divergence).



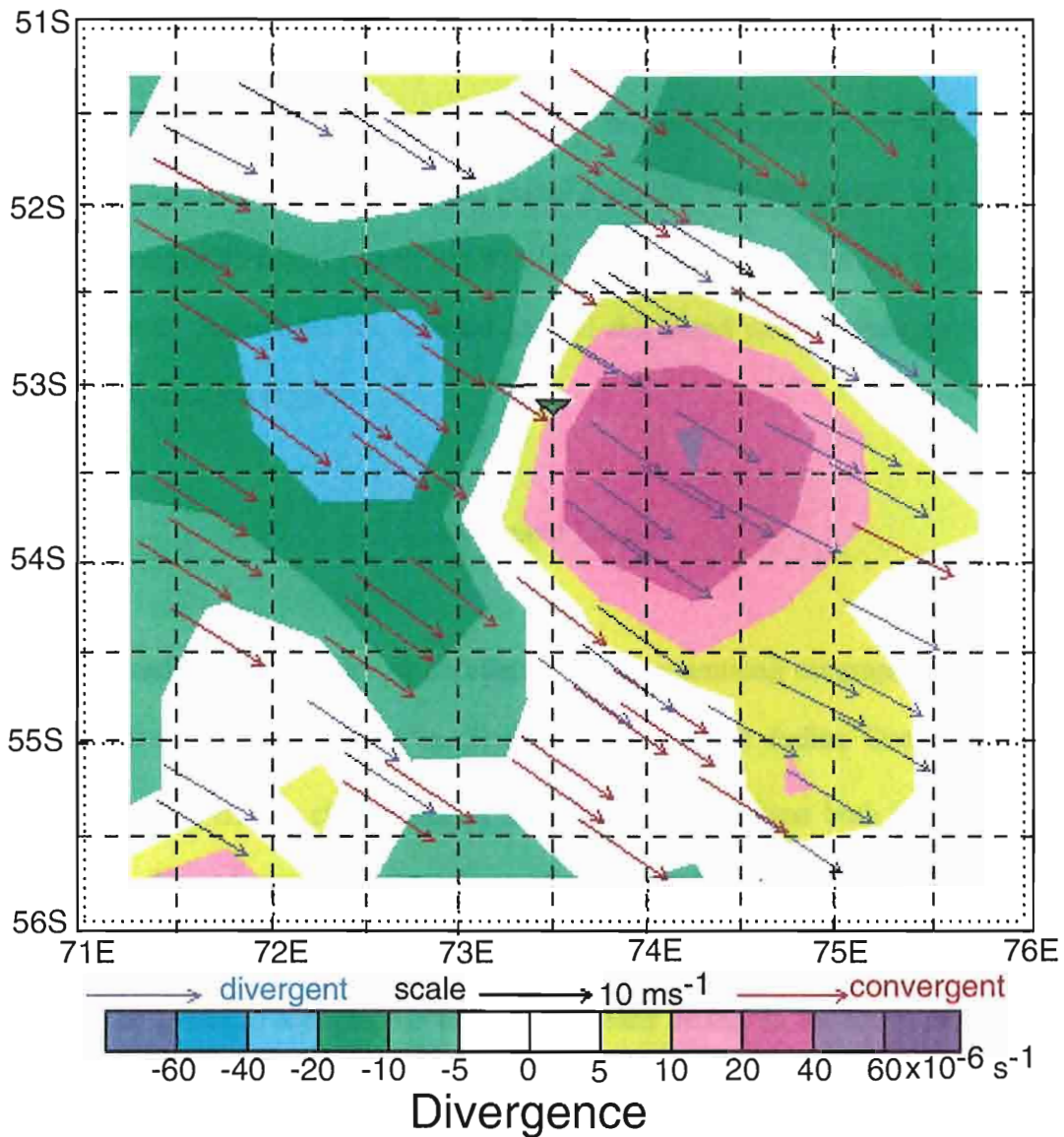


Fig. 2: Divergence field calculated from the NSCAT gridded winds for March 15, 1997 at 12:00 UTC. Divergence is contoured and the wind speeds are proportional to arrow length. The bins used in gridding the NSCAT wind data are outlined by the dashed lines.

technique (Bourassa et al. 1998, 1999). Thus features that exist for a couple of days in the same area are easily captured in the NSCAT animations.

The cause of this vorticity couplet and the divergence pattern is investigated with a simple 1.5-layer reduced gravity atmospheric model with parameters appropriate for the area around Heard Island. Results reveal a similar vorticity pattern in a small area around the modeled island as well as a similar convergent pattern on the windward side of the island. Results on the leeward side of the island do not agree as well and a possible explanation is given.

#### **a. Heard Island**

Heard Island provides an excellent case for examining orographically modified surface winds. Heard Island (Fig. 3) lies in the southern Indian Ocean centered at  $53^{\circ}05' S$   $73^{\circ}30' E$ . The closest islands are small in comparison both horizontally and vertically. The nearest large obstacle to atmospheric flow is the Kerguelen Islands, which are located roughly 450 km to the northwest of Heard Island.

The principle topographic feature of Heard Island is an intermittently active volcano known as Big Ben, whose peak currently reaches 2745 m above sea level (with each eruption, the peak continues to rise). It is roughly conical in shape, with a 22 km diameter at the base. Attached to this base on the Laurens Peninsula is a smaller peak that rises to 715 m. Over 80 percent of the island is covered by glaciers which originate at Big Ben and move relatively quickly (250 meters per year) down the steep slope. The rest of the island is composed of exposed rock surfaces.

at Big Ben and move relatively quickly (250 meters per year) down the steep slope. The rest of the island is composed of exposed rock surfaces.



Fig. 3: Heard Island on a rare clear cloudless day taken by Captain P. Schlossberger of Qantas Airways (photograph courtesy of Australian Antarctic Division).



Heard Island is situated in a belt of strong westerly winds associated with the Antarctic Circumpolar Current and the westerly wind drift. The Australian Antarctic Division provides the following climatological background information for Heard Island at their URL, <http://www.antdiv.gov.au/>. The mean wind speed at Atlas Cove (on the northwest side) is 26 kilometers per hour with 75 percent of the observations being from either the northwest, west, or southwest. Direct sunlight varies from an average of 2.4 hours a day in the Austral summer to 0.8 hours a day in the Austral winter. The average temperature remains close to freezing throughout the year. Higher temperatures have been recorded, but due to hazardous conditions, and an automated weather system that has only recently been deployed, observations have been sparse spatially and temporally.

#### **b. Previous Findings**

Determination of flow near obstacles is important in many fields and is not a new field of study. It is used in designing lift on aircraft wings as well as for creating aerodynamically efficient automobiles. It is required in architecture to build homes and structures which can resist hurricane force winds. Designers of the Alaskan oil pipeline had to use models to test if their structure could safely transport huge oil supplies.

Visualization has been an important method of qualitatively measuring flow around obstacles. It has assisted in understanding the mechanisms behind such important topics as boundary layer separation, vortex shedding, and turbulence. Milton Van Dyke (1982) assembled an excellent collection of photographs used by researchers important topics as boundary layer separation, vortex shedding, and turbulence. Milton Van Dyke (1982) assembled an excellent collection of photographs used by researchers

in studying fluid flow. One photograph is of flow around a circular cylinder at a Reynolds number of 9.6 (Fig. 4). This image resembles the model flows resulting from our modeling study.

Geophysical fluid dynamics textbooks (e.g., Kundu 1990) demonstrate ideal solutions to the flow near different shapes (e.g., cylinders, spheres, flat plates, etc.). One such problem is modeling the flow near a circular cylinder embedded in an irrotational, inviscid fluid. The radial and tangential velocities,  $u_r$  and  $v_\theta$ , respectively are given by

$$u_r = W \left( 1 - \frac{a^2}{r^2} \right) \cos \theta \quad \text{and} \quad v_\theta = -W \left( 1 + \frac{a^2}{r^2} \right) \sin \theta, \quad (1)$$

where  $W$  is the flow's speed in the far field and  $a$  is the radius of the cylinder. For this field, the maximum speed is  $2W$  and it occurs on the sides of the cylinder perpendicular to the flow (Kundu 1990). This solution assumes that the flow does not penetrate the cylinder, but it does move tangentially with respect to it (the free-slip condition). Observations do not agree with this solution for points very close to the boundary. Due to friction, the radial and tangential flow must vanish at the boundary. Solving this type of problem is more complex.

The increase in computer technology over the past several decades now allows computer models to quickly solve these flow problems numerically. With this improvement, atmospheric modelers have created complex models to study the effects of topography, along with other factors (e.g. moisture and/or thermal effects) on three-dimensional flow fields (Schär and Durran 1997; Lloyd and Stansby 1997; Schär and Smith 1993; Smolarkiewicz and Rotunno 1989; Brighton 1978). Lloyd and Stansby dimensional flow fields (Schär and Durran 1997; Lloyd and Stansby 1997; Schär and Smith 1993; Smolarkiewicz and Rotunno 1989; Brighton 1978). Lloyd and Stansby

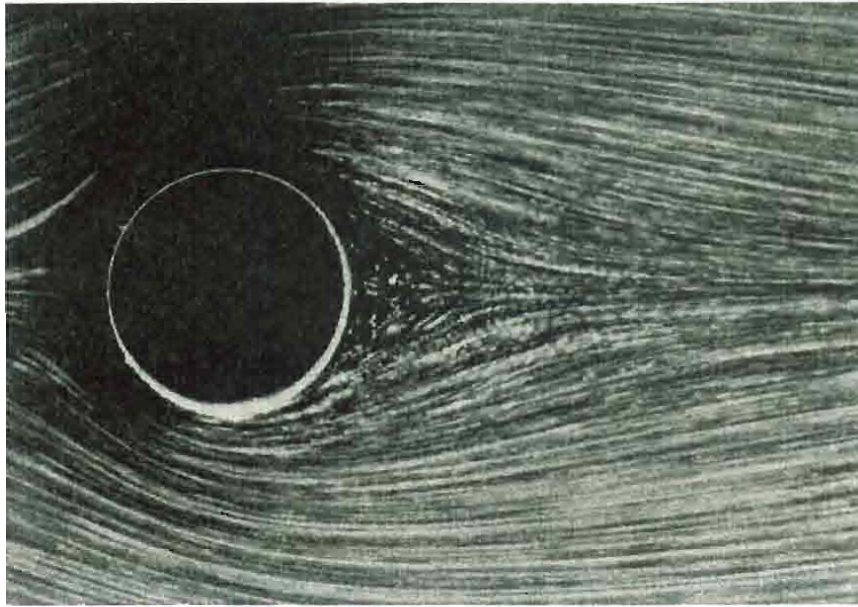


Fig. 4: Circular cylinder at  $R=9.6$  (from Van Dyke 1982). It was developed by moving a cylinder through a tank of water containing aluminum powder and illuminated from underneath. *Photograph taken by Sadatoshi Taneda.*

(1997) performed both numerical models and laboratory studies to examine the unsteady wakes of submerged conical islands in shallow water. As they increased water depth, less vigorous vortex shedding took place. They found that the angle of the island slope exerted little influence on the procedure. Schär and Smith (1993) analyzed shallow water flow past high topography in a nonrotating environment and found three distinct flow regimes: 1) fore-aft symmetry in subcritical conditions; 2) a hydraulic jump over the lee slope in a transition to supercritical flow; and 3) flow separation resulting from the inability of the flow to climb the obstacle. The flow studied herein does not reach the latter stage.

The Reynold's number ( $R$ ) is a measure that compares inertial and frictional forces. In each of the above works  $R$  is high, which leads to turbulent flows in the wake of the obstacle. Herein,  $R$  will remain small, thus we examine the laminar effects of the obstacle to the flow and avoid such aspects as vortex shedding and vortex streets which are not resolved in our gridded NSCAT winds. Also, we develop a more simple model based on the dominant physical principles, while neglecting many of the complexities mentioned above. The goal is to recreate the patterns found in the NSCAT wind fields using a simpler model that captures the physics but requires less computer time.

A simple 1.5-layer atmospheric reduced gravity model is developed (Section 2) to simulate the pattern found in NSCAT wind fields. This model is applied to two case studies with different island shapes: one as a semi-infinite cylinder extending from the surface through all layers of the model; the second has a sloping island bottom from the surface to 1000 m and a cylinder above this height (Section 3). Model results compare favorably to the patterns found in the NSCAT data (Section 4). surface to 1000 m and a cylinder above this height (Section 3). Model results compare favorably to the patterns found in the NSCAT data (Section 4).

Few studies exist that use satellite observations to depict vorticity production due to orographic effects. Lack of data coverage and insufficient spatial resolution have restricted this avenue of research. NSCAT provided high quality vector winds with the resolution necessary to observe these effects.

## 2. MODEL

The weather over the ocean surrounding Heard Island is dominated by the westerly wind belt in which it resides. Due to the island's high latitude, cyclones frequently pass over it creating periods of changing structure in the atmosphere. Frontal passages are followed by a period of steady winds which allow the atmosphere to stabilize. For simplicity in the model, it is assumed that this steady wind creates a stable, well-mixed planetary boundary layer (where the potential temperature is constant with height) under a strong low-level subsidence inversion (Stull 1988). Close to the ocean surface, the potential-temperature profile has a supergeostrophic layer ( $z_0$  to  $z_s$  in Fig. 5 from Lavoie 1974). The well-mixed layer is between this surface layer and a subsidence inversion (heights  $z_s$  to  $h$ ). It is assumed that there is a strong geostrophic wind forcing from the west in the stable layer above the interfacial boundary. This is a commonly adopted model for flow in the marine boundary layer, and it should apply well to the environment around Heard Island.

A simple mixed layer model is used to simulate the vorticity/divergence patterns found in NSCAT gridded data. This model determines if the gross patterns are solely generated by the obstacle. Many researchers have used similar mixed layer models to simulate meso-scale features (e.g. Lavoie 1972; Lavoie 1974; Anthes et al. 1980; Ruscher and Deardorff 1982; Eddington et al. 1992). Following the work of Ruscher simulate meso-scale features (e.g. Lavoie 1972; Lavoie 1974; Anthes et al. 1980; Ruscher and Deardorff 1982; Eddington et al. 1992). Following the work of Ruscher

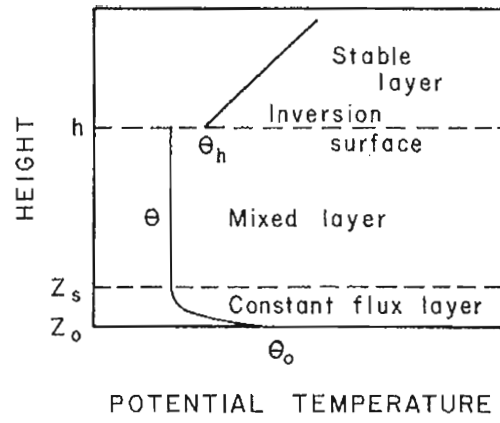


Fig. 5: Model potential-temperature profile (from Lavoie 1974).



and Deardorff (1982), our model neglects the effects of diabatic processes, water vapor, entrainment, and horizontal variations in potential temperature; thereby focusing on the effect of the obstacle (Heard Island) on the boundary layer. The model is an inverse shallow water model (for the atmosphere), with the following governing equations:

$$\frac{\partial \vec{V}}{\partial t} = -\vec{V} \cdot \nabla \vec{V} - f \mathbf{k} \times \vec{V} - g' \nabla h - \frac{C_D |\vec{V}| \vec{V}}{h - z_s} + K \nabla^2 \vec{V} + \frac{\vec{\tau}}{\rho(h - z_s)} \quad \text{and} \quad (2)$$

$$\frac{\partial(h - z_s)}{\partial t} = -\nabla \cdot [\vec{V}(h - z_s)] \quad , \quad (3)$$

where  $\vec{V}$  is the velocity vector and  $h - z_s$  is the depth of the boundary layer. In Eq. (2), the first right hand term is advection, and the second is the Coriolis term (on a  $f$ -plane). The third term is a pressure gradient term, with  $g'$  representing a reduced gravity dependent on the vertical difference in potential temperature ( $\theta$ ) at the inversion:  $g' = g\Delta\theta/\theta$ . The fourth term is a measure of the surface drag in the system with  $C_D$  as the drag coefficient. The surface drag is not a dominant term in the solution. The fifth term is the diffusion (or friction) term with an eddy diffusivity coefficient ( $K$ ), and the last term is the kinematic stress between the two layers in the model. The stable layer above the interface is assumed to be strongly geostrophic with winds moving from west to east because of the westerly wind drift. This kinematic stress is utilized to drive the lower layer. The coefficients listed in the equations are given the following values:

$$f = 2\Omega \sin \phi = 2(2\pi/86400\text{s}) \sin(-53^\circ 5') \approx -1.163 \times 10^{-4} \text{s}^{-1}$$

$$g' = 9.8 \text{ ms}^{-2} \times (15 \text{ K}/275 \text{ K}) \approx .535 \text{ ms}^{-2}$$

$$C_D = 1.2 \times 10^{-3}$$

$$\vec{\tau} = \tau^{(x)} \hat{\mathbf{i}} + \tau^{(y)} \hat{\mathbf{j}}, \quad \tau^{(x)} \approx 3.1 \text{ kgm}^{-1} \text{s}^{-2} \quad \tau^{(y)} = 0.$$

$$C_D = 1.2 \times 10^{-3}$$

$$\vec{\tau} = \tau^{(x)} \hat{\mathbf{i}} + \tau^{(y)} \hat{\mathbf{j}}, \quad \tau^{(x)} \approx 3.1 \text{ kgm}^{-1} \text{s}^{-2} \quad \tau^{(y)} = 0.$$



### a. Stretched Coordinates

The model is gridded on a stretched cylindrical coordinate system centered at the center of the island to accelerate time integration, reduce the memory requirements, and to have higher resolution in our area of interest. The radial component ( $q$ ) is a logarithmic function of the radius:  $q = \ln(r/r_0)$ , where  $r_0$  is the radial location at which the no-slip boundary condition is enforced. The velocity and acceleration vectors in this system become:

$$\bar{\mathbf{V}} = r_0 e^q u^{(q)} \hat{\mathbf{e}}_q + r_0 e^q v^{(\theta)} \hat{\mathbf{e}}_\theta \quad \text{and} \quad (4)$$

$$\frac{d\bar{\mathbf{V}}}{dt} = r_0 e^q \left( \left( u^{(q)} \right)^2 + \frac{\partial u^{(q)}}{\partial t} - \left( v^{(\theta)} \right)^2 \right) \hat{\mathbf{e}}_q + r_0 e^q \left( 2u^{(q)} v^{(\theta)} + \frac{\partial v^{(\theta)}}{\partial t} \right) \hat{\mathbf{e}}_\theta, \quad (5)$$

where  $u^{(q)}$  and  $v^{(\theta)}$  are the radial and tangential velocities in the new system (with units of per second) and  $\hat{\mathbf{e}}_q$  and  $\hat{\mathbf{e}}_\theta$  are the unit normal vectors in the radial and tangential directions, respectively (from this point on the velocity superscripts will be dropped). In this system, the grid has a higher resolution near the island and a coarser resolution in the far field.

The model equations, (2) and (3), are written in the new coordinate system in terms of their radial and tangential components which creates a set of 3 equations (two velocity equations and one layer thickness equation). Next, the time derivatives of  $u$  and  $v$  are separated from the other acceleration terms given in Eq. (5) and placed alone on the left hand side of the velocity equations. The model is set into a transport form using:

the left hand side of the velocity equations. The model is set into a transport form using:

$$u \frac{\partial H}{\partial t} + H \frac{\partial u}{\partial t} = \frac{\partial U}{\partial t} \quad \text{and} \quad (6)$$

$$v \frac{\partial H}{\partial t} + H \frac{\partial v}{\partial t} = \frac{\partial V}{\partial t} , \quad (7)$$

where the variable  $H$  has been used in place of  $h - z_s$ , and capital variables ( $U$  and  $V$ ) represent radial and tangential transport terms in the stretched coordinate system (e.g.  $U = uH$ ). Equations (8) through (10) are the final form of the model equations.

$$\begin{aligned} \frac{\partial U}{\partial t} = & -\frac{4U^2 + V^2}{H} - \frac{\partial(U^2/H)}{\partial q} - \frac{\partial(UV/H)}{\partial \theta} + fV - \frac{g'H}{r_0^2 e^{2q}} \frac{\partial(H + z_s)}{\partial q} \\ & - \frac{C_D r_0 e^q U \sqrt{U^2 + V^2}}{H^2} + \frac{KH}{r_0^2 e^{2q}} \left[ \frac{U}{H} + 2 \frac{\partial(U/H)}{\partial q} + \frac{\partial^2(U/H)}{\partial q^2} \right] , \quad (8) \\ & + \frac{KH}{r_0^2 e^{2q}} \frac{\partial^2(U/H)}{\partial \theta^2} + \frac{\tau^{(x)} \cos \theta + \tau^{(y)} \sin \theta}{r_0 e^q \rho} \end{aligned}$$

$$\begin{aligned} \frac{\partial V}{\partial t} = & -\frac{5UV}{H} - \frac{\partial(UV/H)}{\partial q} - \frac{\partial(V^2/H)}{\partial \theta} - fU - \frac{g'H}{r_0^2 e^{2q}} \frac{\partial(H + z_s)}{\partial \theta} \\ & - \frac{C_D r_0 e^q V \sqrt{U^2 + V^2}}{H^2} + \frac{KH}{r_0^2 e^{2q}} \left[ \frac{V}{H} + 2 \frac{\partial(V/H)}{\partial q} + \frac{\partial^2(V/H)}{\partial q^2} \right] , \text{ and } (9) \\ & + \frac{KH}{r_0^2 e^{2q}} \frac{\partial^2(V/H)}{\partial \theta^2} + \frac{-\tau^{(x)} \sin \theta + \tau^{(y)} \cos \theta}{r_0 e^q \rho} \end{aligned}$$

$$\frac{\partial H}{\partial t} = -2U - \frac{\partial U}{\partial q} - \frac{\partial V}{\partial \theta} . \quad (10)$$

The eddy diffusivity coefficient ( $K$ ) in Eqs. (8) and (9) is a function of the grid size,  $\Delta x$ ; however, in a stretched coordinate system, this term is dependent on radial location. In common two-dimensional diffusive problems where  $\Delta x = \Delta y$ , a simple constraint on choosing the diffusion coefficient is

$$\frac{K \Delta t}{(\Delta x)^2} < \frac{1}{4} \quad (11)$$

$$\frac{K \Delta t}{(\Delta x)^2} < \frac{1}{4} \quad (11)$$

(O'Brien 1986). With this constraint applied to the stretched coordinate system,  $K$  is dependent on the square of the radial distance:

$$K = K_0 \left( \frac{r}{r_0} \right)^2 = K_0 e^{2q}, \quad (12)$$

where  $K_0$  is the value of the diffusion at the island boundary (in this model,  $K_0 = 3000 \text{ m}^2\text{s}^{-1}$ ). Thus, when placed in (8) and (9), the diffusion term is no longer dependent on radial distance ( $q$ ).

The spatial grid used for model integration is an Arakawa scheme C, which is chosen over other schemes (e.g. scheme B) for its ease in calculating certain derivatives, the better structure it gives for short waves, and its superior dispersion characteristics (Arakawa and Lamb 1977). This scheme is staggered with the radial transport, tangential transport, and layer height values computed at different locations. The island border is set at a radius where radial transports ( $U$ ) are calculated; consequently, all layer thickness values are outside the island.

The model equations are integrated on a 75 radial points by 75 tangential points grid. This grid has been chosen so that the grid spacing in the radial direction is equal to the grid spacing in the tangential direction. With the stretched coordinate system, the resolution near the inner boundary, located at  $r = r_0 = 6992.7 \text{ m}$ , is about 600 m in real space or

$$2\Delta q = 2\Delta\theta = 2\pi/75 \approx .084$$

in the stretched coordinate system, whereas locations in the far field are much farther apart. The purpose for the obscure boundary location will become clear when we look at the stretched coordinate system, whereas locations in the far field are much farther apart. The purpose for the obscure boundary location will become clear when we look at

the second case study (Section 3). The resolution at the inner boundary is approximately 450 times greater than the resolution of the outer boundary.

### **b. Temporal and Spatial Differencing**

A centered difference, or leap-frog, scheme is utilized for temporal differencing. A time step of 2.5 s satisfies the CFL condition (see Appendix B). Every 77 time steps, a forward difference is implemented to dampen out the unstable computational mode generated by the leap-frog scheme.

An averaging scheme was used for the spatial differencing of (8) through (10). For example, the first term on the right hand side of (8) requires a value of  $V$  at the same location as a  $U$  value. We use an average of the 4 surrounding  $V$  values to obtain an approximation for  $V$ . A similar averaging is done for the approximation of  $U$  values in Eq. (9). For  $H$  values, an average of the two adjacent grid values is applied for both (8) and (9). In (10), averages of the two adjacent  $U$  and  $V$  values are applied.

### **c. Boundary Conditions**

The boundary condition at the island is no slip. Due to the staggered grid, no tangential transport term lies directly on the boundary. Inside the boundary there is a ring of grid points used in the finite differencing evaluation of the model. As a result, a value must be given to the transports inside the boundary. We assign values that are equal and opposite to the transport on the grid point just outside the boundary, thereby

insuring that an average transport along the boundary will be zero. These internal transport values are required in the diffusion term as well as the radial advection term in Eqs. (9) and (10). The radial transport term is set to a constant zero on the boundary.

The far field boundary condition is an open boundary, which requires that waves and information propagating from the interior of the domain pass through the outer boundary without reflection. The most accurate way to define the outflow for a hyperbolic system is to use the Sommerfeld radiation condition (13) at the boundary (Orlanski 1976):

$$\frac{\partial \psi}{\partial t} + C \frac{\partial \psi}{\partial x} = 0, \quad (13)$$

where  $\psi$  represents any variable and  $C$  is that variable's phase speed. Generalization of (13) to a vector form for use in the stretched coordinate system is:

$$\frac{\partial \vec{V}}{\partial t} + \vec{C} \cdot \nabla \vec{V} = 0. \quad (14)$$

Separating (14) into radial and tangential components leads to

$$r_0 e^q \left( u^2 + \frac{\partial u}{\partial t} - v^2 \right) + r_0 e^q C \left( u + \frac{\partial u}{\partial q} \right) = 0, \text{ and} \quad (15)$$

$$r_0 e^q \left( 2uv + \frac{\partial v}{\partial t} \right) + r_0 e^q C \left( v + \frac{\partial v}{\partial q} \right) = 0. \quad (16)$$

The radial phase speed,  $C$ , is estimated using the transport values just inside the boundary. An inflow condition occurs when  $C < 0$  and an outflow condition occurs, when  $C > 0$ . To alleviate the reflection of the gravity wave back into the domain, Camerlengo and O'Brien (1980) arbitrarily set the phase speed for an inflow condition Camerlengo and O'Brien (1980) arbitrarily set the phase speed for an inflow condition

equal to zero while the outflow condition is set equal to  $2\Delta q/\Delta t$ . A new boundary value is then computed by placing the estimated phase speed in Eqs. (15) and (16):

$$u^{B,n+1} = u^{B,n-1} - 2\Delta t \left[ \left( (u^{B,n})^2 - (v^{B,n})^2 \right) - C \left( u^{B,n} + \frac{u^{B,n} - u^{B-1,n}}{2\Delta q} \right) \right] \text{ and } (17)$$

$$v^{B,n+1} = v^{B,n-1} - 2\Delta t \left[ \left( 2u^{B,n}v^{B,n} \right) - C \left( v^{B,n} + \frac{v^{B,n} - v^{B-1,n}}{2\Delta q} \right) \right], \quad (18)$$

where the superscripts  $B$  and  $n$  represent a point on the boundary at time level  $n$ , and  $B-1$  represents a point just inside the boundary. A similar condition is enforced on the height term. The only difference is that it is governed by the scalar equation (13). The forecast equation for the height field at the outer boundary is:

$$H^{B,n+1} = H^{B,n-1} - 2\Delta t C^{(q)} \left( \frac{H^{B,n} - H^{B-1,n}}{2\Delta q} \right). \quad (19)$$

By using a circular domain, the tangential boundary condition is periodic. Calculations requiring a point on the other side of the  $\theta = 0, 2\pi$  boundary just use a point already calculated in the domain. This means that we only have one open boundary in our domain as opposed to the four which must be defined in a rectangular grid. It also avoids the problem of defining boundaries at corners both for the open boundary and for the closed boundary at the island.

#### d. Model Spinup

The model is spunup from rest using a wind forcing in the upper layer. This forcing is transmitted to the lower layer, with an initial depth of 2000 m, through the

The model is spunup from rest using a wind forcing in the upper layer. This forcing is transmitted to the lower layer, with an initial depth of 2000 m, through the



wind stress term ( $\tau$ ) in Eqs. (8) and (9). This depth is chosen for several reasons: 1) the marine layer surrounding the island is assumed fairly stable with strong steady winds and 2) to insure that the boundary layer does not encroach into the cone slope found in the cone-cylinder test case (a special case used to approximate island topography in the model).

The maximum value of the wind stress is chosen such that when the model reaches equilibrium, the bottom layer wind speed upstream of the island is approximately  $8 \text{ ms}^{-1}$  (for a derivation of the mean layer wind speed refer to Appendix B). The stress is ramped over time in order to diminish the effect of gravity wave production throughout the domain. The time amplitude function, or *TAF*, governing this ramping is:

$$TAF = \frac{e^{At} - 1}{e^{At_0} + e^{At}}, \quad (20)$$

where  $A$  is a constant which controls the ramping's slope and  $t_0$  is the time when the model is through approximately half of the spinup. In this case, we have chosen the following parameter values:  $A = 2 \times 10^{-5} \text{ s}^{-1}$  and  $t_0 = 2 \text{ days} = 1.728 \times 10^5 \text{ s}$ .

During model development, we found that ramping the stress along the radiational boundary condition created a false wave that amplified over time and interfered with the inner domain. Thus, a spatial amplitude factor (SAF) is applied to the forcing as a patch over the domain. The stress ramps to full value in a large area around the island, but far enough away from the outer boundary to prevent this wave's development. The SAF is defined as

development. The SAF is defined as

$$SAF = \frac{1}{1 + e^{B(x-x_0)}} \times \frac{1}{1 + e^{C(y-y_0)}} , \quad (21)$$

where  $B$  and  $C$  are constants (equal to  $9.6 \times 10^{-6}$  and  $1.2 \times 10^{-5}$  in this case) which controls the fall off rate of the patch, and  $x_0$  and  $y_0$  represent the radial location where the function is at half the total value. The values of  $x_0$  and  $y_0$  are set such that the maximum forcing is within a square whose center is the island and whose sides have a length of 1000 km.

One necessity of a new model code is that it must remain stable long enough into its integration to make valid physical inferences. Many checks for stability are available. One is an inspection of the total energy. The equation for total energy,  $TE$ , is:

$$TE = \frac{1}{2} \int_A (u^2 + v^2 + g'H) H dA , \quad (22)$$

where  $A$  is the total area of integration. Some oscillations in  $TE$  after spinup are expected as the model stabilizes. A large change, or an exponential increase, in  $TE$  is not desired. Another simple factor to check is the total mass, which is verified using the sum of the heights throughout the domain. These tests and visual studies of the data did not reveal anything to diminish confidence in the model results.



### 3. CASE STUDIES

Two separate case studies are performed using the model. The only difference between the two cases is in the bottom topography near the island boundary. The first case employs a cylindrical obstacle as the island boundary, thus it only has a flat bottom topography. The second case has an axisymmetric sloping bottom that leads up to a cylindrical obstacle. The latter case better represents the conical shape of Heard Island and should better represent the flow field around the island.

#### a. Cylindrical Obstacle

A cylindrical obstacle is the simplest internal boundary to model in this stretched cylindrical coordinate system. It is merely a wall that blocks the flow in the lower layer. This representation is consistent with Heard Island's height of 2745 m, which pierces the atmospheric boundary layer modeled at a height of 2000 m. The radius of the cylinder is set at 6992.7 m; the mean radius corresponding to a height of 1000 m on Heard Island.

The resulting flow field (Fig. 6) is similar to that seen in laboratory experiments for low Reynold's number flow (Fig. 4). The winds on the west side come in at a speed of around  $8 \text{ ms}^{-1}$ . Note the dual maxima on the north and south sides of the for low Reynold's number flow (Fig. 4). The winds on the west side come in at a speed of around  $8 \text{ ms}^{-1}$ . Note the dual maxima on the north and south sides of the

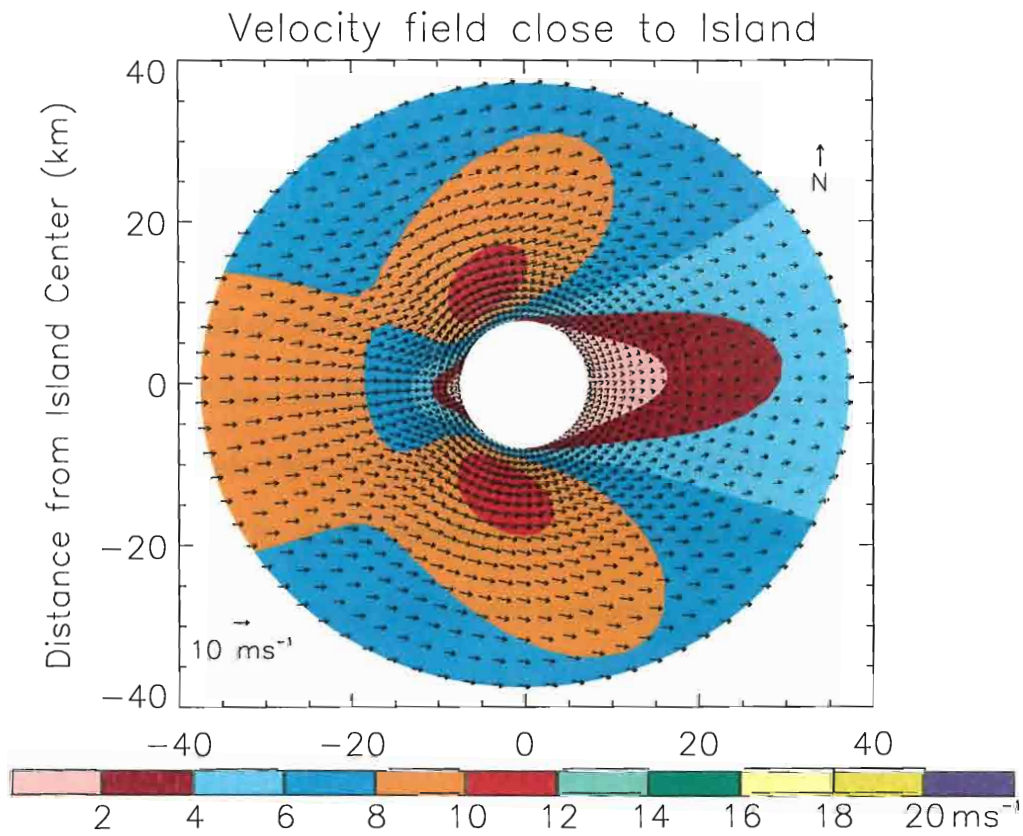


Fig. 6: Flow field around cylindrical obstacle after a spinup of 9 model days. The wind speed is depicted by the background color. The length of the wind arrows is directly proportional to the wind speed. The direction referred to as north in the paper is given in the upper right hand corner.

island, as expected from the analytical solution to the problem [Eq. (1)]. An area of weaker flow is evident on the leeward side of the island, indicating that the Reynold's number of the flow is on the order of 5. This approximation is based both on comparisons to laboratory experimental flow fields, depicted in Van Dyke's *Album of Fluid Motion* (1982), and to the numerical definition of  $R$ . This definition is given by:

$$R = \frac{UL}{K} \quad (23)$$

where  $U$  is the speed of the flow approaching the obstacle and  $L$  is the length scale of the obstacle. Since  $K$  increases by the square of the ratio between radial location and the radius of the cylinder boundary,  $R$  is largest at the cylinder boundary and it rapidly decreases away from it. At the boundary ( $r = r_0$ ),  $R$  has a value of approximately 37. For a point at  $r = 3r_0$  this value drops down to about 4.

The Coriolis effect is apparent in the location of the wind maxima. The southern lobe is a little farther east and not as large as the northern lobe. In general the wind vectors on the southern side of the domain are of a slightly larger magnitude than those on the northern side. Model runs with no Coriolis (not shown) have a symmetric maxima around the island. This feature is also model time dependent. As the model progresses through spinup, the winds to the left of the obstacle have a higher magnitude and the flow is from the southwest to the northeast. Eventually, the winds and their associated maxima turn clockwise (in the figure's reference frame), and they reach the west to east flow field visible in Fig. 6.

The effect of Coriolis also appears in the vorticity field (Fig. 7) as a slight rotation of the vorticity pattern. The positive area extends slightly further east than the

The effect of Coriolis also appears in the vorticity field (Fig. 7) as a slight rotation of the vorticity pattern. The positive area extends slightly further east than the

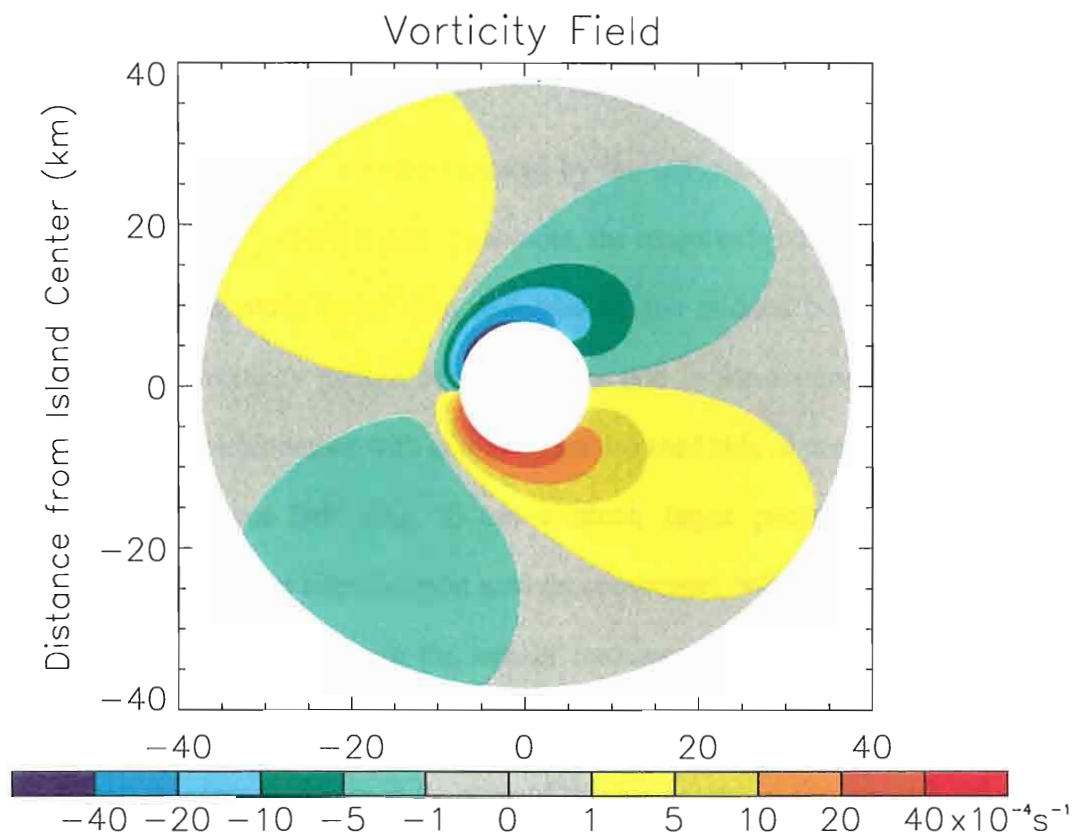


Fig. 7: Vorticity field around cylindrical obstacle after a spinup of 9 model days. Note the size of the maxima on each side of the obstacle when compared to the size of the maxima in Fig. 1. Note also the magnitude of the maxima (around  $61 \times 10^{-4} \text{ s}^{-1}$ ).

negative area. The overall pattern detected here is not nearly as large as that seen in the NSCAT gridded vorticity fields (Fig. 1) and it is elongated downstream. The island signal in the vorticity extends out for at least 100 km in the NSCAT fields, whereas the strongest model fields ( $|\text{Vorticity}| > 10^{-4} \text{ s}^{-1}$ ) only extend out to at most 40 km. This can be attributed to a smearing effect created by the  $0.5^\circ \times 0.5^\circ$  spatial binning used in deriving the NSCAT gridded winds. Also note, the magnitude of the modelled vorticity is 2 orders of magnitude larger than observed by the gridded NSCAT winds. The extension of the vorticity pattern downstream is due to the asymmetry beginning to form at low Reynolds number with eddies on the leeward side of the model island.

The divergence field (Fig. 8) has a much larger pattern than the vorticity anomaly. The windward side is almost entirely convergent with a small exception very close to the island boundary. In the area of maximum winds on the northwest and southwest sides of the island, the field is strongly divergent. Weaker magnitude divergence/convergence occurs in the area of weaker winds on the leeward side of the island. This does not agree with the NSCAT animations on the leeward side of the domain.

Examination of the boundary layer depth anomaly throughout the model domain (not shown) reveals evidence of the geostrophic adjustment the model performed during spinup. Positive anomalies are on the northeast side of the grid while negative anomalies are on the southwest side. There is also a mass buildup on the windward side of the obstacle (Fig. 9). This maxima extends northward into the higher values on the northeast side of the domain. The area on the leeward side of the island is the northeast side of the domain. The area on the leeward side of the island is

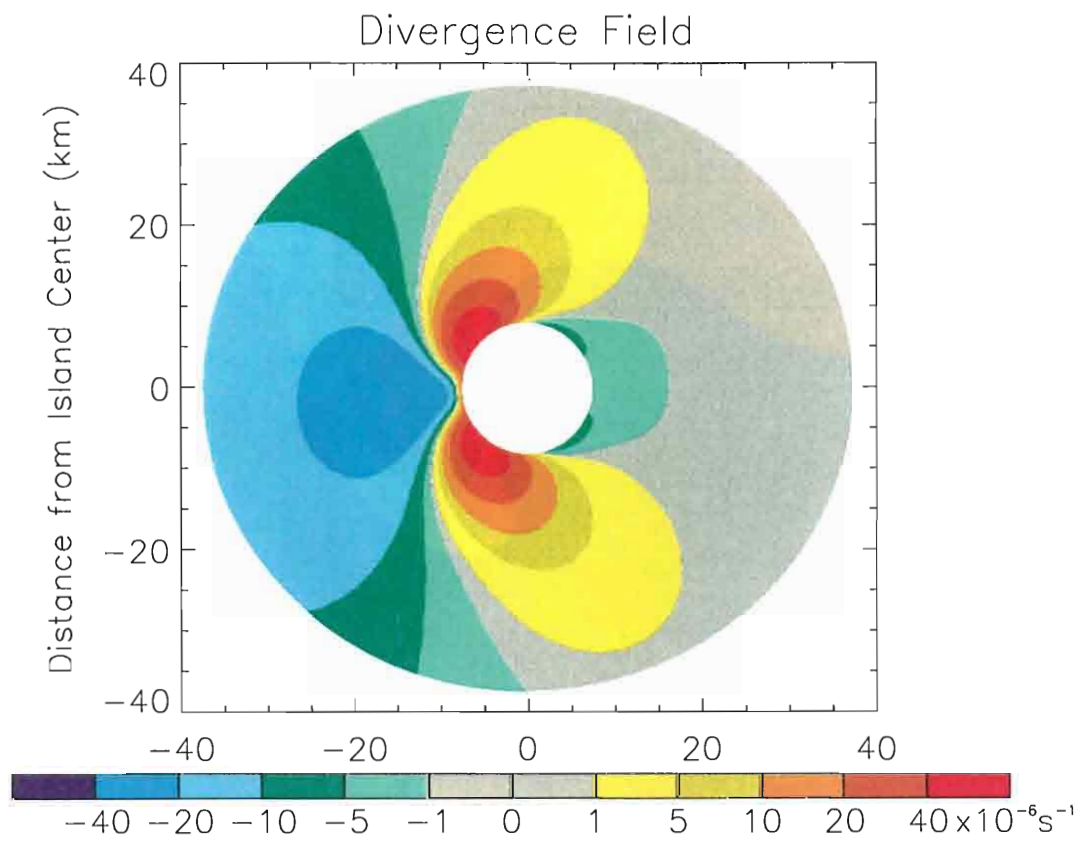


Fig. 8: Divergence field around cylindrical obstacle after a spinup of 9 model days. Note that the maximum divergence in the field is  $67 \times 10^{-6} \text{s}^{-1}$  whereas the maximum convergence is  $36 \times 10^{-6} \text{s}^{-1}$ .



Boundary Layer Depth Anomaly--Near Island

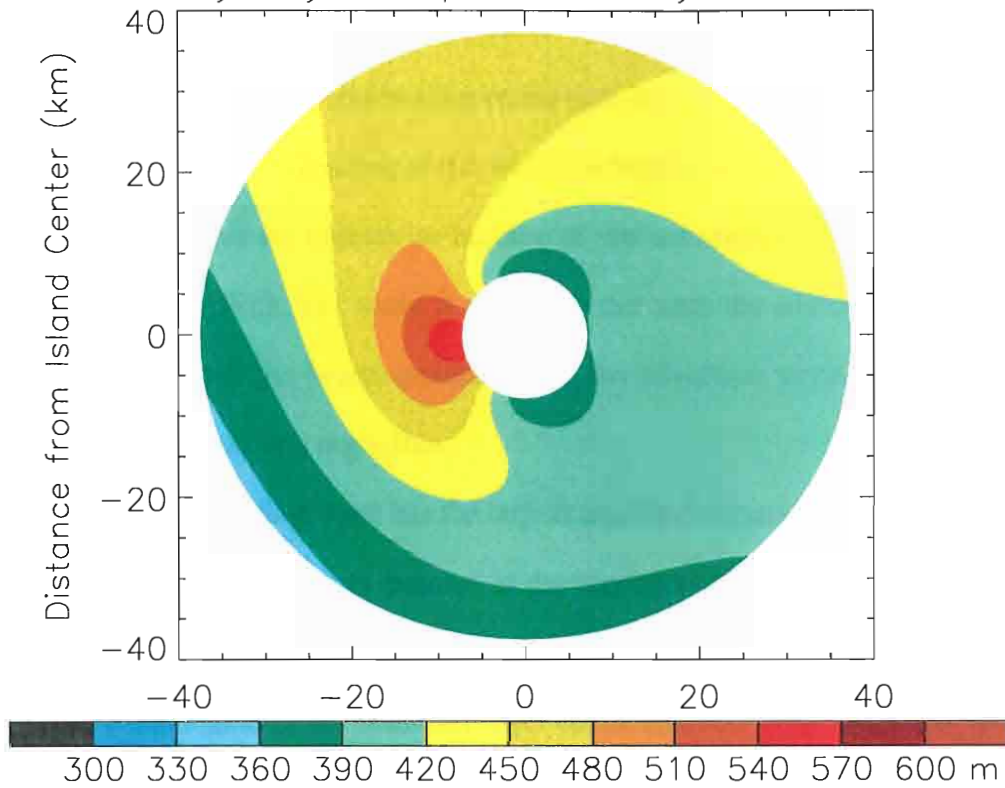


Fig. 9: Boundary layer depth anomaly from the initial state after a spinup of 9 model days.

comparatively flat. A shallow area lies near this leeward boundary with two minima on the northeast and southeast coasts of the obstacle.

The physical processes responsible for maintaining this wind field are examined by studying the along-trajectory accelerations. These accelerations are obtained at each grid point by projecting the acceleration vector onto the wind vector and determining the component that is in the direction of the wind (Eddington et al. 1992). We can assume that the wind vectors are trajectories because of our assumption that the model is in a near steady state. With this study it is shown that near the island three components dominate the model: the height gradient term, the advection terms, and the diffusion terms. The drag term was negligible.

The height gradient term has the largest amplitude of any of the other terms and therefore is the most dominant process in developing and maintaining the wind speed maxima on the northwestern and southwestern sides of the obstacle. We expect this from our examination of the boundary layer depth anomaly (Fig. 9). This term also decelerates the flow in the region between these two maxima and in the area on the leeside of the obstacle. The advection term is opposite in sign and generally reduced in magnitude from the height gradient term. This indicates that this term is attempting to advect the wind speed maxima region further downstream of the flow. The diffusion term affects only the area within 5 to 10 km of the boundary. This term decelerates the flow in the area of the wind speed maxima. This is as expected since the diffusion process acts to spread out any local maxima into its surrounding regions.

Thus, this basic case study has recreated a similar pattern to that observed in the NSCAT gridded data. The largest magnitude vorticity is in a pattern to the right and left

Thus, this basic case study has recreated a similar pattern to that observed in the NSCAT gridded data. The largest magnitude vorticity is in a pattern to the right and left



of the flow (positive to the right and negative to the left). Upstream a weaker magnitude signal is found in the vorticity with opposite sign. How does the addition of a sloping topography change the model?

### **b. Combined Cone and Cylinder Obstacle**

The second case study includes a sloping bottom topography below a height of 1000 m, and a cylinder above this height. The goal is to more closely approximate the topography of Heard Island without having to use a scheme in which the interface rides up and down the island (which Ruscher and Deardorff (1982) call an 'encroachment' scheme). The cone has a diameter of 22 km (approximately the parameters for Heard Island). The radius of the cylinder is equal to that in the first case. The cone, extending the radius of the surface from 6.9927 km to 11 km. The choice of the cylinder radius is arbitrary, but required to prevent the modeled boundary layer from encroaching down to the cone boundary. Any changes in the wind field between cases (a) and (b) are due to this change in topography.

The resulting wind field (Fig. 10) clearly shows an increase in the magnitude of the maxima on the north and south sides of the obstacles. This is the area of the greatest difference between the two models (Fig. 11), where the maxima are increased by 1.25  $\text{ms}^{-1}$ . This can be attributed to the momentum principle (Kundu 1990). The fluid has less depth to travel through so it must respond by forcing the fluid through the area at a faster speed.

faster speed.

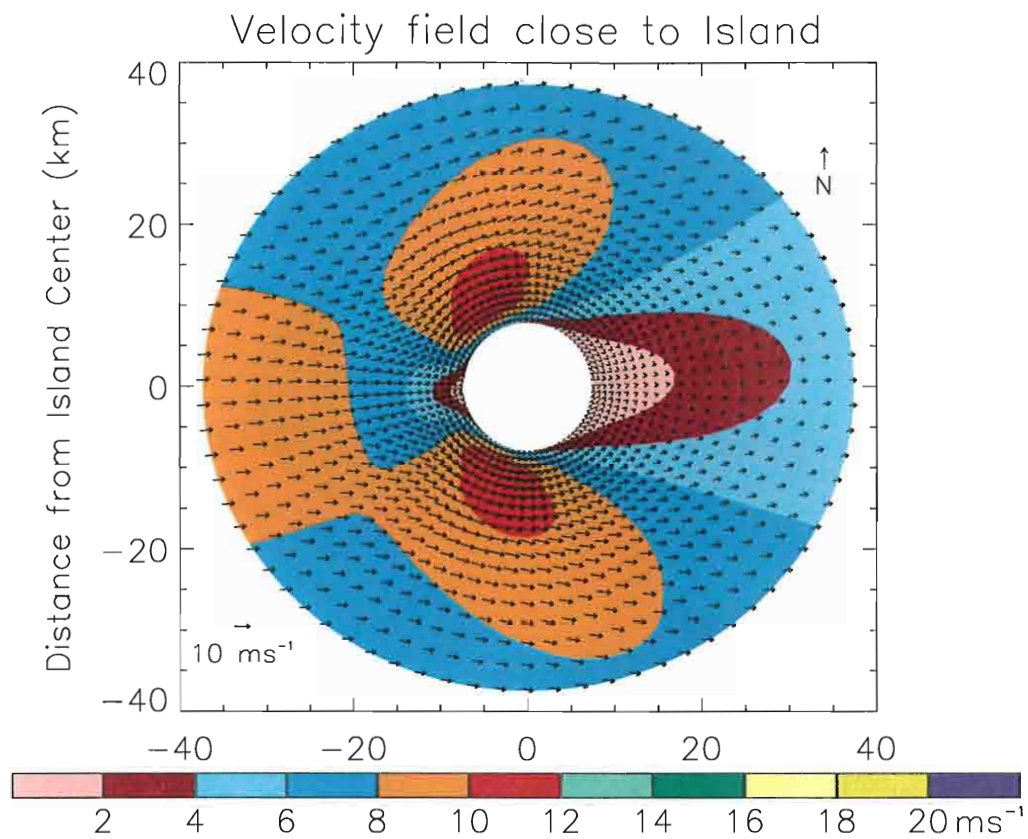


Fig. 10: Flow field around cone/cylinder obstacle after a spinup of 9 model days. The wind speed is depicted by the background color. The length of the wind arrows is directly proportional to the wind speed. The direction referred to as north in the paper is given in the upper right hand corner.

### Velocity Field Difference Close to Island

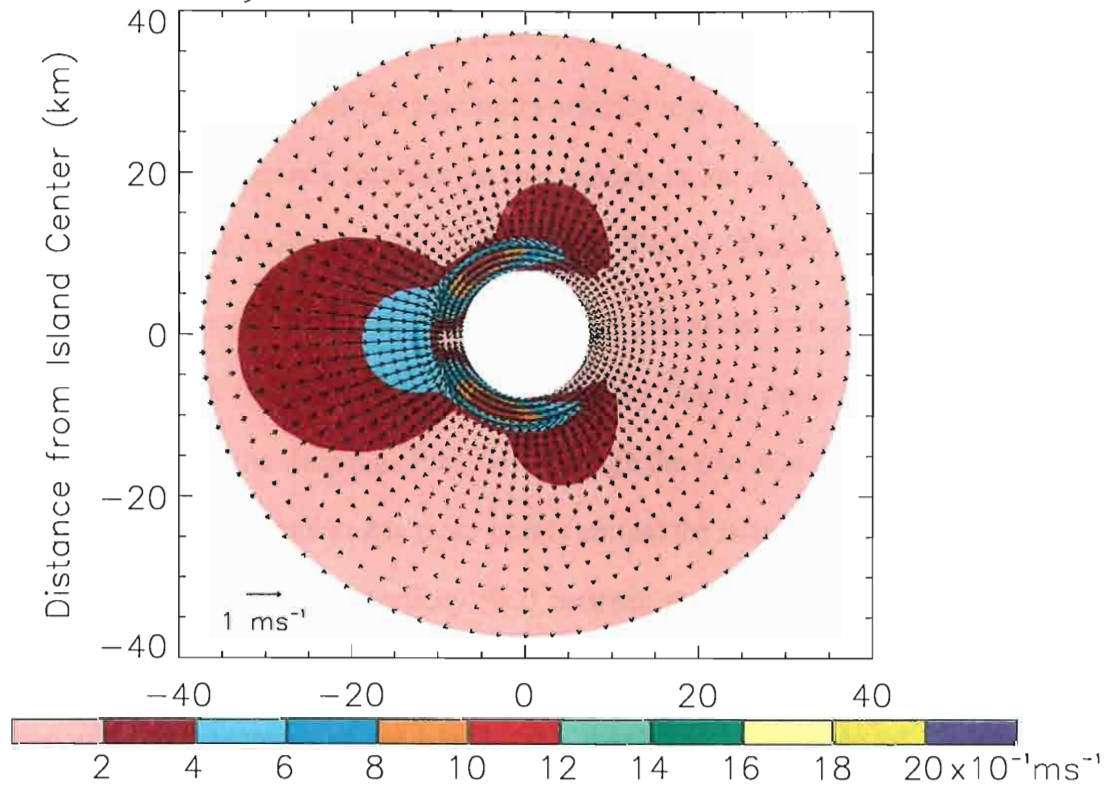


Fig. 11: Velocity field difference for the cylinder wind field minus the cone/cylinder wind field. Note the change in magnitude of the color scale. The largest difference is in the area of the maximum winds on the northwest and southwest sides of the obstacle (around  $1.2 \text{ ms}^{-1}$  faster in the cone/cylinder case than the cylinder case).

Another prominent difference is in the inflow region on the west side of the island. Flow entering this area is around  $.6 \text{ ms}^{-1}$  slower than flow entering the cylinder case. This difference is most important at the base of the cone (the outer radius of the island) on the western tip. Thus, the flow field is sensing the island ahead of it and shunting its transport into the two maximum velocity regions.

A further difference between the two models is an ability of the cone/cylinder model flow to more easily pass around the island. Vector difference magnitudes greater than  $.2 \text{ ms}^{-1}$  are on the north and south sides of the island out to a distance of about 15 km away from the boundary. The difference vector field is away from the boundary. Again this is due to the shunting of the flow through the two wind speed maxima. The cone/cylinder flow appears to stay more tightly around the island in the area .

The difference in the vorticity field between the two cases (Fig. 12) follows directly from the differences in the flow field. Immediately outside of the sloping topography and upstream of the island, the maximum magnitude of the upstream vorticity couplet is reduced by approximately ten percent from the cylinder case (Fig. 7). The difference is a result of the anticyclonic (cyclonic) circulation found on the north (south) portions of the vector difference field (Fig. 11). This change is also caused by the velocity gradient in the direction of the flow on the west side of the island. The winds are reduced as they move over the upslope of the topography and then they move into a region of greater maximum wind speed. This vorticity difference indicates that our cone/cylinder topography is an improvement over that found in the cylinder case study. The resulting vorticity field now more resembles that seen in the NSCAT study. The resulting vorticity field now more resembles that seen in the NSCAT

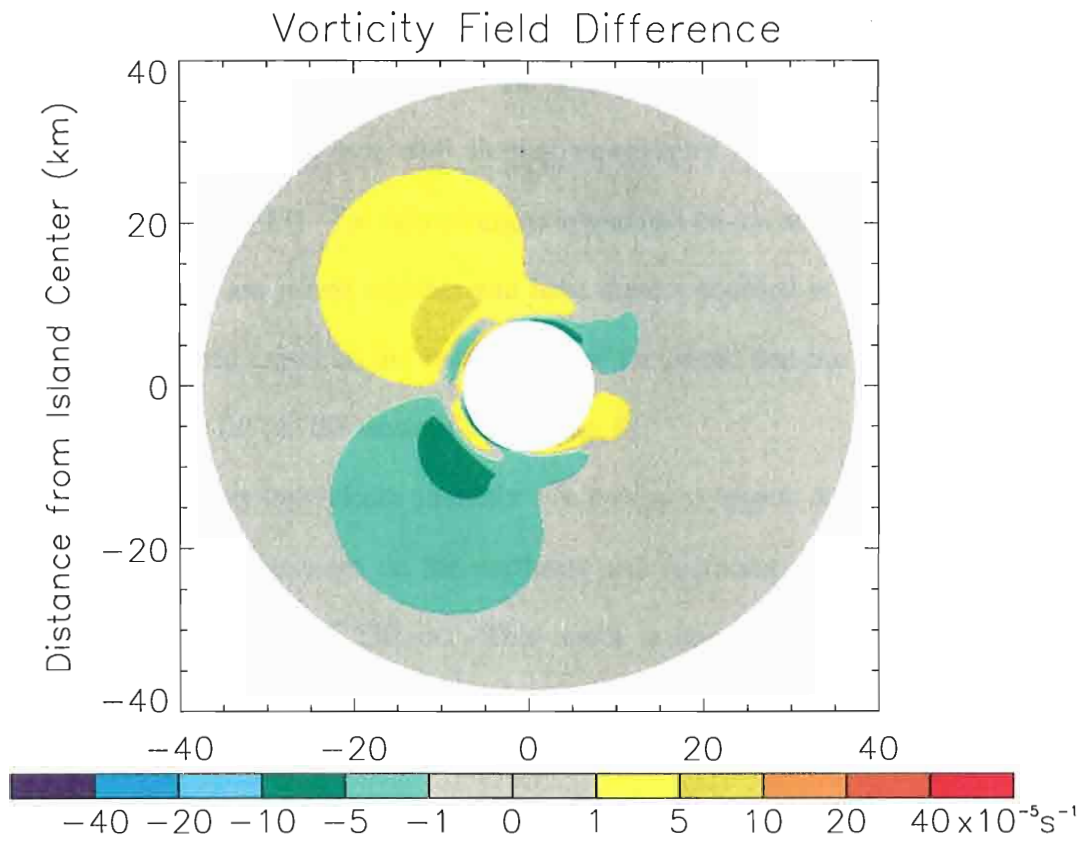


Fig. 12: Vorticity field difference for the cylinder vorticity minus the cone/cylinder vorticity. Note the changes in the magnitude of the color table. Also note that the negative colors on the south side of the domain indicate that the vorticity in the cone/cylinder case are more positive on the south side (and vice versa on the north side).

gridded data (which except for strong steady winds does not represent the upstream vorticity couplet).

The magnitude of the change in the vorticity field is small compared to that of the divergence field. The area with sloping topography has a dramatically changed divergence field (Fig. 13). The two divergence maxima on the northwest and southwest sides of the island are joined together and have almost doubled in magnitude. A large area of convergence exists on the eastern side of the island and has almost double the magnitude in case (a) (on the western side of Fig. 8).

The boundary layer depth anomaly's (not shown) largest difference between the two cases is that the minima on the northeast and southeast sides of the island are stronger, 210 m instead of 230 m. This result is consistent with the wind speed maxima in these areas and the height gradient term dominating the model.



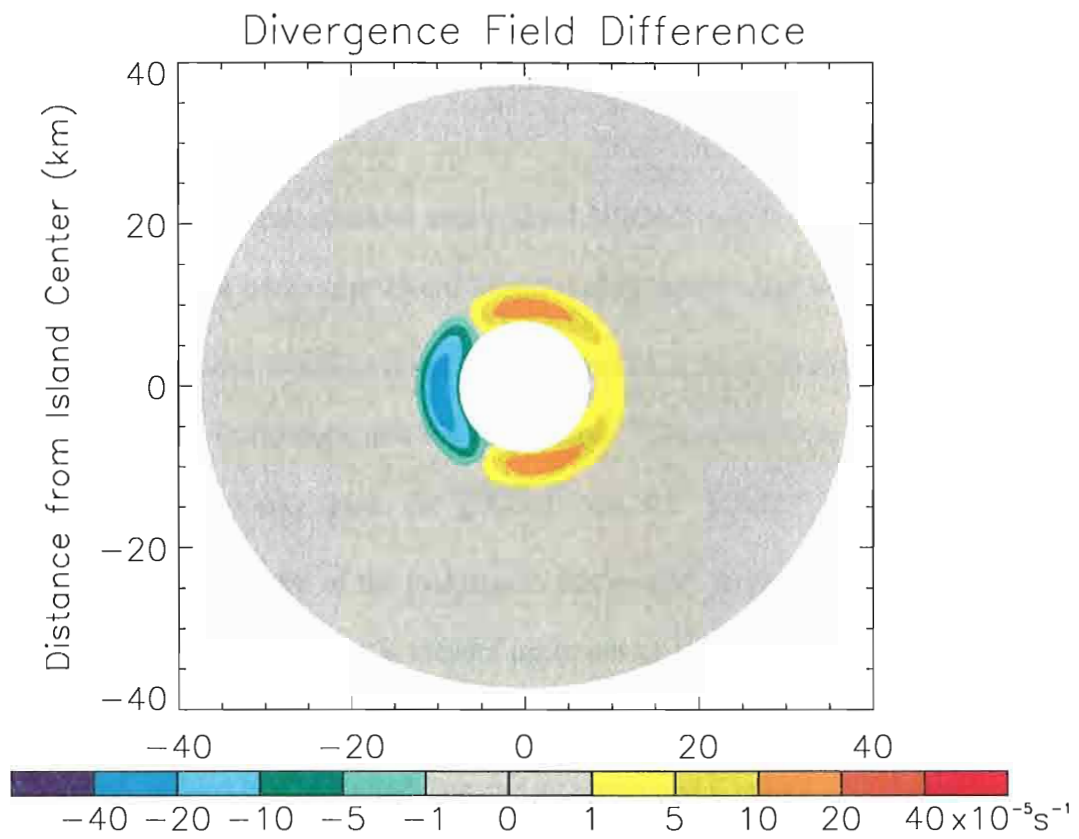


Fig. 13: Divergence field difference for the cylinder case minus the cone/cylinder case. Notice that the color bar represents values that are an order of magnitude larger than those in the cylinder divergence (Fig. 8).



#### 4. DISCUSSION

A simple numerical model and gridded NSCAT winds show fields of vorticity and divergence that occur near Heard Island during steady state wind conditions. For weaker constant layer winds ( $< 8 \text{ ms}^{-1}$ ) in our model, a large positive/negative vorticity couplet is created to the right and left of the flow. This couplet is apparent in a large percentage of the cases from the gridded NSCAT winds. For stronger flows ( $> 8 \text{ ms}^{-1}$ ), the magnitude of the maxima in this couplet increases; however, a weaker, and oppositely signed maxima is created upstream of this couplet. This pattern is also apparent in the NSCAT data during periods of strong winds.

The gridded NSCAT wind data and its associated vorticity and divergence fields reveal that the primary vorticity couplet occurs around Heard Island in approximately 47% of the NSCAT observation period. The divergence pattern shows up even more often, approximately 59% of the time. The two patterns coincide in about 34% of the period. The patterns usually occur after a large area of negative vorticity (low pressure in the southern hemisphere) passes through the domain. This finding is expected since strong and steady winds typically follow frontal passage.

One distinct difference between the modeled data and the gridded NSCAT data is in the magnitude of the vorticity and divergence features. The modeled vorticity maxima is on the order of  $610 \times 10^{-5} \text{ s}^{-1}$  (for the pictured field in Fig. 7) while the

gridded NSCAT vorticity maxima never exceeds  $6 \times 10^{-5} \text{ s}^{-1}$ . The difference is similar, but a bit less dramatic for the divergence. The maximum modeled divergence is on the order of  $27 \times 10^{-5} \text{ s}^{-1}$  (for the cone/cylinder case) while the gridded NSCAT divergence never exceeds  $6 \times 10^{-5} \text{ s}^{-1}$ . There is one main reason for this difference: a land mask extending 25 km from land (based on a  $1/12^\circ$  resolution field), was placed on the NSCAT swath data to eliminate signal contamination due to land. For Heard Island, the landmask is approximately a circle of radius 36 km centered at the center of the island. The largest magnitude vorticity and divergence values lie within 5 km of our cylinder boundary, or at a location 12 km away from the center of the domain. Thus, the largest magnitude vorticity could not be seen by NSCAT.

With such a large land mask placed over the most important features in our vorticity and divergence fields, one wonders how the gridded NSCAT data can resolve such a feature at all. A look at the methodology used to grid the NSCAT swath data reveals part of the answer to this question. The swath data are temporally averaged (Bourassa et al. 1999) and spatially binned into  $0.5^\circ \times 0.5^\circ$  grid boxes that have endpoints on the multiples of half degrees (e.g.  $73.5^\circ \text{ E}$ ,  $52.0^\circ \text{ S}$ , see Fig. 2). Since no additional spatial smoother is added, whatever feature is present will be enlarged to the domain of grid boxes it resides in. The largest magnitude modelled vorticity feature ( $|\text{Vorticity}| > 10^{-4} \text{ s}^{-1}$ ) extends out to around a 40 km distance from the island. If this feature is split into two boxes in the grid, it would appear to be 100 km large.

As for the divergence, the windward side of the domain appears to correctly model the convergence of flow going into the island. However, on the leeward side, the  
As for the divergence, the windward side of the domain appears to correctly model the convergence of flow going into the island. However, on the leeward side, the

NSCAT divergence field tends to indicate a large area of divergence and the model signal is much weaker and smaller. One possibility is that the binning technique employed to grid the data has spread out the divergence maxima on the north and south sides of the island into a larger area. The points in the middle would then be an addition of components from both maxima. This theory is acceptable assuming that the divergence fields are larger in size than that modeled.

Another theoretical explanation is that the wind maxima on the north and south sides of the island are producing swell that propagate downstream. This swell could be affecting the winds found by NSCAT; however, this seems unlikely to produce large errors since a scatterometer is designed to measure backscatter from capillary waves and very short gravity waves on the ocean surface (Naderi et al., 1991).

Another difference between the modeled vorticity and the gridded NSCAT vorticity is the size of the maxima. The gridded NSCAT vorticity data on average has a couplet that extends outward to around 100 km. The highest magnitude modeled vorticity contour ( $> 10^{-4} \text{ s}^{-1}$ ) extends out to at most 40 km from the island center. If we look out beyond this range, the sign of the couplet remains the same on the leeward side of the domain. One reason for the larger area of the maxima in the NSCAT data is the smoothing performed by binning the winds in the  $0.5^\circ \times 0.5^\circ$  grid. The wind field surrounding Heard Island and the vorticity associated with it is being spread out into several grid boxes; thereby, artificially enlarging the pattern.

Another possible explanation is that the model is not correctly determining the size of the maxima. This could be due to several factors, such as the parameters used to run the model. The reduced gravity ( $g'$ ) is based on a stable inversion between our two

layers. Since upper air measurements over Heard Island are nonexistent during the period of NSCAT, we had to give both an approximate  $\Delta\theta$  and an approximate initial height for the boundary layer.

The eddy diffusivity coefficient ( $K$ ) may be inappropriate because its range of values is limited by model constraints rather than a match to physical observations. It is a coefficient required in numerical models to dampen out computational noise. The value chosen for this project lies well within the constraints placed upon  $K$  in Eq. (12); however, we develop  $K$  as a function of the square of the radius due to the stretched coordinate system. This leads to values of  $K$  which are very large only a short distance from the island (e.g. at 5 cylinder radii from the island,  $K = 25K_0$ ). Large values in the far field force the strongest winds to remain in the center of the domain. This problem may be acceptable for the application we have chosen here; however, this model would be poor for larger scale problems.

The strength of the wind speed approaching the island also has an effect on the size and shape of the vorticity fields. For weaker wind speeds than those used in the two case studies, both vorticity couplets decreased in magnitude. The pattern for the couplet immediately around the boundary moved more upstream and looked more east-west symmetric (i.e., not elongated downstream). For stronger winds, both vorticity couplets increased in magnitude. The gradient between the two couplets also increased in the area of the wind speed maxima on the northwest and southwest sides of the boundary. The shape of the couplet around the island became much more elongated downstream.

downstream.

Another factor that could explain the size of the maxima is the model topography. A slight expansion of the vorticity maxima is found in the sloping topography in the cone/cylinder case. Perhaps the vorticity couplet signal would spread out if the actual topography of Heard Island were included. This could be accomplished by creating a few more layers to the model that actually allowed the top of the mountain to be submerged. An encroachment scheme would have to be employed for this type of model to work.

Despite these problems, this is the first time that vorticity and divergence signals like this have been resolved by a satellite. Study of mesoscale features like these vorticity and divergence couplets have been made practical through the NSCAT program. Programs such as NSCAT and the now operational SeaWinds on QuikSCAT have opened up a new field of study in meso-scale atmospheric and oceanic applications. These observations should lead to better atmospheric and coupled models which give us a more complete understanding of our ocean-atmosphere system.

## 5. CONCLUSIONS

A simple inverse shallow water model for atmospheric flow is developed to examine the physics behind vorticity and divergence couplets often found in the NSCAT wind data around small islands (e.g., Heard Island). The model is integrated on a stretched cylindrical coordinate grid to highlight features near the inner boundary.

Two case studies highlight the impact of modelled island topography. The first case had a flat topography near the island, and a solid infinitely tall cylindrical wall at a set radius from the center of the island. The second case had the same central wall, but it is surrounded by a sloping bottom surface that merged with the sea at a radius comparable to the sea-level radius of Heard Island.

A vorticity couplet similar to that observed by NSCAT was created very close to the island and extended downstream in the cylinder case. Another couplet was created upstream of the island and had an opposite sign. The size and location of these couplets depend strongly on the velocity of the winds coming towards the island. For lighter winds, the upstream couplet is very weak and the couplet surrounding the island is more east-west symmetric. For stronger winds, the magnitude of both couplets increase. The positive/negative couplet closest to the island is pushed more downstream while the opposite sign couplet increases in size.

opposite sign couplet increases in size.



An area of convergence is found upstream of the island with strong divergence in the area of maximum wind speeds (to the right and left of the island in the flow field). Weak divergence is found downstream and has a much smaller magnitude than the upstream convergence. The location of the divergence maxima in the gridded product is explained by the binning technique employed in the NSCAT winds. We also hypothesize that it could be related to the wind speed maxima on the north and south sides of the island creating swell, which then propagate downstream, interact with the short waves, and thus alter the backscattered signal picked up by NSCAT.

The cone cylinder case featured similar results, but had stronger maximum winds to the right and left of the flow near the island and weaker winds coming into the island. The vorticity field extends slightly further west and the maximum vorticity very close to the island is decreased. The change in divergence is centered over the topography and the outer field is basically unaffected. The upstream vorticity couplet is reduced in magnitude around ten percent, implying an improvement over the cylinder case study.

The model was able to demonstrate the basic features observed by NSCAT. The land mask placed on the swath data does not allow NSCAT to pick up the strongest magnitude vorticity/divergence features close to the island, but it is able to retrieve a signal of the overall pattern. This demonstrates another success of NSCAT in observing meso-scale features.



**APPENDIX A**  
**COORDINATE TRANSFORMATION**

The governing equations are transformed from a Cartesian  $(x, y)$  coordinate system to a polar  $(q, \theta)$  coordinate system with a stretched radial component defined by

$$q = \ln\left(\frac{r}{r_0}\right) = \ln\left(\frac{\sqrt{x^2 + y^2}}{r_0}\right) \text{ and } \theta = \tan^{-1}\left(\frac{y}{x}\right). \quad (\text{A1})$$

Inverting (A1) to solve for  $x$  and  $y$  results in

$$x = r_0 e^q \cos \theta \quad \text{and} \quad y = r_0 e^q \sin \theta. \quad (\text{A2})$$

These  $x$  and  $y$  coordinates are used to define a position vector.

$$\vec{\mathbf{R}} = x\hat{\mathbf{i}} + y\hat{\mathbf{j}} = r_0 e^q \cos \theta \hat{\mathbf{i}} + r_0 e^q \sin \theta \hat{\mathbf{j}}, \quad (\text{A3})$$

where  $\hat{\mathbf{i}}$  and  $\hat{\mathbf{j}}$  are the unit normal vectors in the Cartesian coordinate system.

The unit normal vectors in the new coordinate system can be defined using this position vector:

$$\hat{\mathbf{e}}_q = \frac{\frac{\partial \vec{\mathbf{R}}}{\partial q}}{\left| \frac{\partial \vec{\mathbf{R}}}{\partial q} \right|} = \cos \theta \hat{\mathbf{i}} + \sin \theta \hat{\mathbf{j}} \quad \text{and} \quad \hat{\mathbf{e}}_\theta = \frac{\frac{\partial \vec{\mathbf{R}}}{\partial \theta}}{\left| \frac{\partial \vec{\mathbf{R}}}{\partial \theta} \right|} = -\sin \theta \hat{\mathbf{i}} + \cos \theta \hat{\mathbf{j}} \quad (\text{A4})$$

Solving for the new unit normal vectors in terms of the Cartesian vectors and replacing them in the position vector gets  
Solving for the new unit normal vectors in terms of the Cartesian vectors and replacing them in the position vector gets

$$\vec{\mathbf{R}} = r_0 e^q \hat{\mathbf{e}}_q \quad (\text{A5})$$

The velocity and acceleration vectors are then derivatives of this position vector. A difficulty in changing coordinate systems is that the unit normal vector's derivative must be considered.

$$\vec{\mathbf{V}} = \frac{d\vec{\mathbf{R}}}{dt} = \frac{d(r_0 e^q)}{dt} \hat{\mathbf{e}}_q + r_0 e^q \frac{d\hat{\mathbf{e}}_q}{dt}, \quad (\text{A6})$$

where

$$\frac{d\hat{\mathbf{e}}_q}{dt} = -v \sin \theta \hat{\mathbf{i}} + v \cos \theta \hat{\mathbf{j}} = v \hat{\mathbf{e}}_\theta, \quad (\text{A7})$$

and  $u$  and  $v$  will represent the radial and tangential velocities ( $\dot{r}$  and  $r\dot{\theta}$ ) in the stretched coordinate system. Replacing this derivative gives,

$$\vec{\mathbf{V}} = r_0 e^q u \hat{\mathbf{e}}_q + r_0 e^q v \hat{\mathbf{e}}_\theta \quad (\text{A8})$$

The acceleration vector is determined using the fact that  $\frac{d\hat{\mathbf{e}}_\theta}{dt} = -v \hat{\mathbf{e}}_q$ :

$$\frac{d\vec{\mathbf{V}}}{dt} = r_0 e^q \left( u^2 + \frac{\partial u}{\partial t} - v^2 \right) \hat{\mathbf{e}}_q + r_0 e^q \left( 2uv + \frac{\partial v}{\partial t} \right) \hat{\mathbf{e}}_\theta. \quad (\text{A9})$$

**APPENDIX B**  
**VARIOUS NECESSARY CALCULATIONS**

**1. Calculation of Layer Wind**

We want to calculate a mean layer wind for the bottom layer in the model (the lower 2000 meters). To do this calculation, I must account for the log wind profile which occurs close to the surface. The NSCAT winds are calibrated to height of 10 meters. From the wind animations, the average wind speed is about 7 meters per second (which corresponds well to the mean winds found near the surface at Atlas Cove).

The log wind profile is governed by the equation:

$$u(z) = \frac{u_*}{k} \ln\left(\frac{z}{z_0}\right). \quad (\text{B1})$$

For  $u(10 \text{ m}) \approx 7 \text{ ms}^{-1}$ ,  $u_* \approx .25 \text{ ms}^{-1}$  is a friction velocity,  $k \approx .40$  is the von Karman constant, and  $z_0 \approx .0001 \text{ m}$  is the roughness length. We assume that this log-wind profile exists from the surface to a height of around 50 meters. Beyond this height, the wind speeds are assumed constant and equal to  $u(50 \text{ m})$ . Integrating this  $u$  over the entire layer and then dividing by the height of the layer results in a mean layer wind.

entire layer and then dividing by the height of the layer results in a mean layer wind.

$$\bar{U} = \frac{\int_{z_0}^{50 \text{ m}} \frac{u_*}{k} \ln\left(\frac{z}{z_0}\right) dz + \int_{50 \text{ m}}^H \frac{u_*}{k} \ln\left(\frac{50 \text{ m}}{z_0}\right) dz}{H - z_0} \quad (\text{B2})$$

For the above values and for a layer height of 2000 meters, the mean wind is approximately equal to  $8.19 \text{ ms}^{-1}$ .

## 2. Check of CFL Condition

The maximum velocity vector expected in the model is the mean layer wind in the lower layer plus the gravity wave speed. We are driving the model to reach a maximum layer wind speed of around 20 meters per second (on the north and south sides of the island). The gravity wave speed is calculated by

$$\sqrt{g'H} = \sqrt{(9.81 \text{ ms}^{-1}) \left( \frac{15 \text{ K}}{275 \text{ K}} \right) (2000 \text{ m})} = 32.7 \text{ ms}^{-1} \quad (\text{B3})$$

Therefore, the maximum velocity ( $c$ ) that we expect is  $52.7 \text{ ms}^{-1}$ . Transformed into  $q$ -space at a point closest to the boundary (where the velocity in the transformed space would be a maximum), this speed is

$$c = 7.54 \times 10^{-3} \text{ s}^{-1}.$$

Transformed into  $q$ -space, the new eddy-diffusivity coefficient becomes:

$$K = 6.14 \times 10^{-5} \text{ s}^{-1}$$

The CFL condition for an advection-diffusion problem is defined numerically as

$$\frac{2c^2(\Delta t)^2 + 4K\Delta t}{(\Delta q)^2} \leq 1 \quad (\text{B4})$$

$$\frac{2c^2(\Delta t)^2 + 4K\Delta t}{(\Delta q)^2} \leq 1 \quad (\text{B4})$$

Replacing the known values, we can solve for a range of  $\Delta t$  which is numerically stable. In this case,  $\Delta t \leq 2.99$  s.

## **APPENDIX C**

### **SCATTEROMETRY**

Scatterometers on polar orbiting satellite platforms are designed to measure near-surface wind velocities over oceans during almost any kind of weather conditions (Naderi et al. 1991). Scatterometers, along with other types of satellite observations, supplement an oceanic surface wind observation network that currently is sparse and based on ships of opportunity and buoys (both drifting and stationary). In-situ data also suffer from problems with instrumentation, ship motions, and transmission errors that must be taken into account (Smith et al. 1999). Scatterometers have the advantages of improved coverage and less observational uncertainty.

Scatterometers transmit microwave pulses to the surface and measure the backscattered power received by the satellite. Different frequencies in the microwave range have been used by different satellites (e.g. Seasat operated at a frequency of 14.6 GHz (Ku-band), the European Space Agency's Remote-Sensing Satellites (ERS-1/2) used a 5.3-GHz (C-band) signal and the NASA Scatterometer (NSCAT) had a 13.995 GHz (Ku-band) signal). As the beam hits the ocean surface, its interaction with the water waves is key to determining wind velocity. Wind stress over the ocean creates waves that roughen the sea surface. The wavelength of the microwaves is such that they interact with capillary waves (ripples) and very short gravity waves. There is a waves that roughen the sea surface. The wavelength of the microwaves is such that they interact with capillary waves (ripples) and very short gravity waves. There is a

relationship between sea surface roughness, observing angle, wind speed and direction, and signal frequency that is connected to the normalized radar cross section,  $\sigma_0$ . Changes in the surface roughness affect the radar cross section which in turn modifies the magnitude of the backscattered signal.

The first successful satellite scatterometer was the Seasat scatterometer (SASS) of 1978. With it came millions of calibrated  $\sigma_0$  measurements that were used to refine the geophysical model function for velocity. This is not to say that there is a single known transfer function for determining wind speed and direction, as there are several complexities. Beaudoin et al. (1996) points out that the details defining these relationships are among the most challenging problems in geophysical fluid dynamics: atmospheric stability, wave generation, electromagnetic propagation and interaction theory. They also note that white caps on high wind waves serve to complicate the calculation. Furthermore, rain drops creating ripples on the ocean surface affect observations collected by scatterometers (Bliven et al., 1993), particularly those with shorter wavelength (e.g. Ku-band).

Despite these difficulties, it is still possible to calculate wind velocities from a scatterometer to within a reasonable accuracy. However, in order to calculate a velocity, one  $\sigma_0$  measurement is not enough; multiple spatial and temporal colocated measurements are necessary. A second antenna on the satellite which looks at the sea surface from a different azimuth direction assists in determining wind direction. This second observation will give four possibilities for the wind direction; one which is the correct value and one which is  $180^\circ$  out of phase. A third look at the same location results in a much better chance of selecting the correct direction. With these



observations and other ambiguity removal algorithms, an accurate wind direction can be determined by scatterometers (Bourassa et al. 1997).

The NASA Scatterometer (NSCAT) flew aboard the Japanese Advanced Earth Observational Satellite (ADEOS) launched in August of 1996. It was a polar orbiter with antenna scanning the front, side, and back on each side of the satellite, and two polarizations on one of these beams, thus creating up to four colocated measurements for each wind vector retrieval. Data were obtained on both sides of the satellite in 600 kilometer swaths, with a resolution of 25 kilometers within the swaths. A 380 kilometer gap existed between the swaths. In two days, NSCAT covers about 90% of the ice-free oceans (Freilich and Dunbar 1999).

NSCAT 10-meter wind speeds and directions were highly accurate (Bourassa et al. 1997; Freilich and Dunbar 1999). NASA's original goal with NSCAT was to provide a product with root mean square differences of less than  $2 \text{ ms}^{-1}$  and 20 degrees for wind speed and direction, respectively. These studies compared NSCAT winds with high resolution in-situ observations, and found uncertainties of around  $1.5 \text{ ms}^{-1}$  and 15 degrees (for correctly selected ambiguities, which is approximately 90% correct selection). This precision at high resolution was an incredible leap forward in our ability to observe the ocean. There are many applications in both meteorology and oceanography which benefit from this technology. Monthly mean ocean surface wind fields derived from NSCAT observations in coastal and equatorial regions were resolved better than those found by the European Center for Medium-Range Weather Forecasts (ECMWF) operational numerical weather prediction models (Liu et al. 1998). It can also give new insight on mesoscale problems such as the influence of Forecasts (ECMWF) operational numerical weather prediction models (Liu et al. 1998). It can also give new insight on mesoscale problems such as the influence of

hurricane Marco on the gap flow in the Chivela Pass Bourassa et al. (1999), and other central American passes (Chelton et al. 1999 a, b).

Unfortunately, ADEOS failed in June of 1997, thus limiting data collection to eight and a half months. Swath data are available from September 19, 1996 to June 28, 1997 with only 10 days of missing observations due to engineering adjustments on the satellite. The success of NSCAT observations has prompted the rapid deployment of a SeaWinds scatterometer on a new satellite, QuikSCAT. As an improvement to NSCAT, QuikSCAT will have a continuous 1800 kilometer swath, eliminating the 380 kilometer nadir gap and extending the outer scanning distance 100 kilometers on each side. It was launched in June of 1999 and has an expected operational lifespan of at least 2 years (Graf et al., 1998).

## REFERENCES

- Anthes, R. A., N. L. Seaman, and T. T. Warner, 1980: Comparisons of numerical simulations of the planetary boundary layer by a mixed-layer and multi-level model. *Mon. Wea. Rev.*, **108**, 365-376.
- Arakawa, A., and V. R. Lamb, 1977: Computational design of the basic dynamical processes of the UCLA general circulation model. *Methods in Computational Physics, Vol. 17*, Academic Press, 174-265, 337 pp.
- Beaudoin, P. T., D. M. Legler, and J. J. O'Brien, 1995: Information content in the ERS-1 three-day repeat orbit scatterometer winds over the North Pacific through March 1992. *Mon. Wea. Rev.*, **124**, 583-601.
- Bliven, L. F. and J. P. Giovanangeli, 1993: An experimental-study of microwave-scattering from rain-roughened and wind-roughened seas. *Int. J. of Rem. Sens.*, **14**, 855-869.
- Bourassa, M. A., L. Zamudio, and J. J. O'Brien, 1999: Noninertial flow in NSCAT observations of Tehuantepec winds. *J. Geophys. Res.*, **104**, 11311-11319.
- Bourassa, M. A., D. M. Legler, J. J. O'Brien, J. N. Stricherz, and J. Whalley, 1998: High temporal and spatial resolution animations of winds observed with the NASA scatterometer. *14th International conference on IIPS*, Phoenix, AZ, American Meteorological Society, 556-559.
- Bourassa, M. A., M. H. Freilich, D. M. Legler, W. T. Liu, and J. J. O'Brien, 1997: Wind observations from new satellite and research vessels agree, *EOS Trans. AGU*, **78**, 597,602.
- Brighton, P. W. M., 1978: Strongly stratified flow past three-dimensional obstacles. *Quart. J. R. Met. Soc.*, **104**, 289-307.
- Camerlengo, A. L. and J. J. O'Brien, 1980: Open boundary conditions in rotating fluids. *J. Comp. Phys.*, **35**, 12-35.
- Chelton, D. B., M. H. Freilich, and S. K. Esbensen, 1999a: Satellite observations of the wind jets off Central America, Part I: Case studies and statistical characteristics.
- Chelton, D. B., M. H. Freilich, and S. K. Esbensen, 1999a: Satellite observations of the wind jets off Central America, Part I: Case studies and statistical characteristics. *Mon. Wea. Rev.*, in press.

- Chelton, D. B., M. H. Freilich, and S. K. Esbensen, 1999b: Satellite observations of the wind jets off Central America, Part II: Regional relationships and dynamical considerations. *Mon. Wea. Rev.*, in press.
- Eddington, L. W., J. J. O'Brien, and D. W. Stuart, 1992: Numerical simulation of topographically forced mesoscale variability in a well-mixed marine layer. *Mon. Wea. Rev.*, **120**, 2881-2896.
- Freilich, M. H. and R. S. Dunbar, 1999: The accuracy of the NSCAT 1 vector winds: Comparisons with National Data Buoy Center buoys. *J. Geophys. Res.*, **104**, 11231-11246.
- Graf, J.E.; Wu-yang Tsi; Jones, L., 1998: Overview of QuikSCAT mission-a quick deployment of a high resolution, wide swath scanning scatterometer for ocean wind measurement, Proceedings IEEE Southeastcon '98 'Engineering for a New Era' (Cat. No.98CH36170), p. xiv+416, 314-17.
- Kundu, P. K., 1990: *Fluid Mechanics*. Academic Press, 638 pp.
- Lavoie, R. L., 1972: A mesoscale model of lake-effect storms. *J. Atmos. Sci.*, **29**, 1025-1040.
- Lavoie, R. L., 1974: A numerical model of trade wind weather on Oahu. *Mon. Wea. Rev.*, **102**, 630-637.
- Liu, W. T., W. Q. Tang, P. S. Polito, 1998: NASA scatterometer provides global ocean-surface wind fields with more structures than numerical weather prediction. *Geophys. Res. Letters*, **25**, 761-764.
- Lloyd, P. M., and P. K. Stansby, 1997: Shallow-water flow around model conical islands of small side slope, Part II: Submerged. *J. Hydr. Engrg.*, **123**, 1068-1077.
- Milliff, R. F., T. J. Hoar, H. van Loon, M. Raphael, 1999: Quasi-stationary wave variability in NSCAT winds. *J. Geophys. Res.*, **104**, 11425-11435.
- Naderi, F. M., M. H. Freilich, and D. G. Long, 1991: Spaceborne radar measurement of wind velocity over the ocean--An overview of the NSCAT scatterometer system. *Proceedings of the IEEE*, **79**, 850-866.
- O'Brien, J. J., 1986: The diffusive problem. *Advanced Physical Oceanographic Numeric Modelling*. D. Riedel Publishing Company, 127-144, 608 pp.
- Ruscher, P. H., and J. W. Deardorff, 1982: A numerical simulation of an atmospheric vortex street. *Tellus*, **34**, 555-566.
- Ruscher, P. H., and J. W. Deardorff, 1982: A numerical simulation of an atmospheric vortex street. *Tellus*, **34**, 555-566.
- Schär, C. and D. R. Durran, 1997: Vortex formation and vortex shedding in continuously stratified flows past isolated topography. *J. Atmos. Sci.*, **54**, 534-554.

- Schär, C. and R. B. Smith, 1993: Shallow-water flow past isolated topography. Part I: Vorticity production and wake formation. *J. Atmos. Sci.*, **50**, 1373-1400.
- Smith, S. R., M. A. Bourassa, R. J. Sharp, 1999: Establishing more truth in true winds, *J. Atmos. and Oceanic Technol.*, **16**, 939-952.
- Smolarkiewicz, P. K., and R. Rotunno, 1989: Low Froude number flow past three-dimensional obstacles. Part I: Baroclinically generated lee vortices. *J. Atmos. Sci.*, **46**, 1154-1164.
- Stull, R. B., 1988: *An Introduction to Boundary Layer Meteorology*. Kluwer Academic Publishers, 666 pp.
- Van Dyke, M., 1982: *An Album of Fluid Motion*. The Parabolic Press, 176 pp.
- Zierden, D. F., M. A. Bourassa, and J. J. O'Brien, 1999: Cyclone surface pressure fields and frontogenesis from NASA Scatterometer (NSCAT) winds. *J. Geophys. Res.*, in press.

## BIOGRAPHICAL SKETCH

### Degrees

1996: B. S. Meteorology and Physics, The Florida State University

### Experience

1993-1996: Pseudo-stress analyst for FSU Pacific Ocean winds set as a  
MASIG (Meso-scale Air-Sea Interaction Group) employee

1995-1996: Undergraduate thesis work entitled, 'Complex Empirical  
Orthogonal Function Analysis in Two Dimensional Data Sets:  
Theory and Examples'

1996: Researched the Indopacific throughflow region under Dr. Tony  
Busalacchi at NASA/Goddard Spaceflight Center during the USRA/  
Graduate Student Summer Program

1996-1998: Worked on quality-control for true winds in ship observations as a  
COAPS (Center for Ocean and Atmospheric Prediction Studies)  
employee

1997-1999: This thesis.

### Honors

National Merit Scholar

National Merit Corporate Scholar- Bridgestone/Firestone

National Merit Scholar

National Merit Corporate Scholar- Bridgestone/Firestone

1994-1996: American Meteorological Society/Industry Undergraduate Scholar

1996: Attended NASA/Goddard Spaceflight Center's USRA/Graduate Student  
Summer Program

1996-1999: National Science Foundation Graduate Research Fellowship

1999-2000: University Fellowship-- The Florida State University

### **Memberships**

American Meteorological Society (AMS)

Chi Epsilon Pi- Meteorology Honor Society

Sigma Pi Sigma- Physics Honor Society

Phi Beta Kappa

### **Personal Information**

Born May 6, 1974 in Lakeland, Florida

Resided in Plant City, Florida (the winter strawberry capital of the world) until  
attending FSU in Fall of 1992

Married January 9, 1999 to Jennifer Elizabeth Townsend in Plant City, Florida

### **Publications**

Sharp, R. J., 1996: Complex Empirical Orthogonal Function Analysis in Two  
Dimensional Data Sets: Theory and Examples. Undergraduate Honors  
Thesis, The Florida State University.

Smith, S. R., M. A. Bourassa, R. J. Sharp, 1999: Establishing more truth in  
true winds, *J. Atmos. and Oceanic Technol.*, **16**, 939-952.